Journal of Power Sources 267 (2014) 78–97

Contents lists available at ScienceDirect

Journal of Power Sources

journal homepage: www.elsevier.com/locate/jpowsour

Damage of cells and battery packs due to ground impact

Yong Xia [a, b, *], Tomasz Wierzbicki [a], Elham Sahraei [a], Xiaowei Zhang [a]

[a] Impact and Crashworthiness Lab, Massachusetts Institute of Technology, 77 Massachusetts Ave, Room 5-218A, Cambridge, MA 02139, USA
[b] State Key Lab of Automotive Safety and Energy, Department of Automotive Engineering, Tsinghua University, Beijing 100084, China

HIGHLIGHTS

- A general methodology is developed for analyzing ground impact of battery pack.
- Scenarios of ground impact against battery pack of electric cars are discussed.
- A hypothetic global FE model is developed for ground impact of battery pack.
- Parametric study is carried out for ground impact of battery pack.
- Failures of individual cell and shell casing are predicted with detailed models.

ARTICLE INFO

Article history:
Received 12 February 2014
Received in revised form
29 April 2014
Accepted 14 May 2014
Available online 23 May 2014

Keywords:
Ground impact
Battery pack
Lithium-ion cell
Multi-level modeling
Fracture
Electric short circuit

ABSTRACT

The present paper documents a comprehensive study on the ground impact of lithium-ion battery packs in electric vehicles. With the purpose of developing generic methodology, a hypothetic global finite element model is adopted. The force–displacement response of indentation process simulated by the global FE model is cross-validated with the earlier analytical solutions. The punching process after the armor plate perforation, the ensuing crack propagation of the armor plate as well as the local deformation modes of individual battery cells are clearly predicted by the global modeling. A parametric study is carried out, and a few underlying rules are revealed, providing important clues on the design of protective structure of battery packs against ground impact. In the next step, detailed FE models at the level of a single battery cell and shell casing are developed and simulations are performed using boundaries and loading conditions taken from the global solution. In the detailed modeling the failure of individual components is taken into account, which is an important indicator of electric short circuit of a battery cell and possible thermal runaway. The damage modes and the deformation tolerances of components in the battery cell under various loading conditions are observed and compared.

© 2014 Elsevier B.V. All rights reserved.

1. Introduction

Protecting lithium-ion cells from crash related damage is a serious concern for vehicle manufacturers. Battery packs in hybrid vehicles are relatively small and they are usually placed in well-protected areas, away from crush zones and possible intrusion of foreign objects. Plug-in hybrids and pure electric cars have much larger battery packs which must be wisely integrated into the vehicle body structure. There are basically two main design concepts: the "T" architecture and the "Floor" architecture (see Fig. 1), each with its own advantages and limitations. In the "T" configuration battery modules are arranged along the tunnel between the seats and in the area of the real axel under the passenger seat, where most of gasoline cars place their fuel tanks. Such architecture, found for example in Fisker Karma, Chevy Volt and Opel Ampera ensures an excellent protection against frontal collision and side impact. But the "T" solution may sometimes compromise passenger comfort and interior space. Still it is not unconditionally safe, as one fire accident following a side collision test prompted NHTSA to launch a full investigation [1].

Placing the battery pack under a vehicle floor lowers the car's center of gravity and leaves an entire interior space for comfortable accommodation of occupants and luggage. It comes though at a price of lowering vehicle ground clearances that could have grave consequences. The "Floor" battery pack configuration is found, amongst others in the BMW i3, Nissan Leafs, Mitsubishi i-Miev,

* Corresponding author. State Key Lab of Automotive Safety and Energy, Department of Automotive Engineering, Tsinghua University, Beijing 100084, China. Tel.: +86 10 62789421.
E-mail address: xiayong@tsinghua.edu.cn (Y. Xia).

http://dx.doi.org/10.1016/j.jpowsour.2014.05.078
0378-7753/© 2014 Elsevier B.V. All rights reserved.

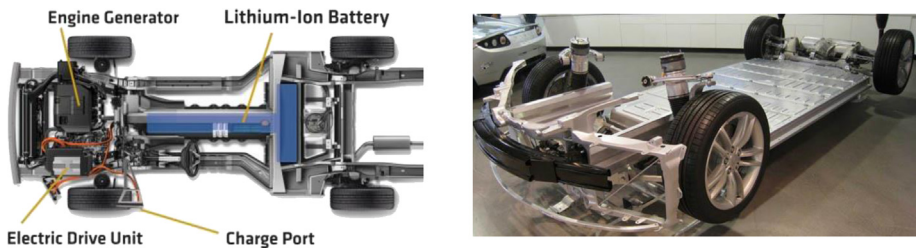

Fig. 1. Battery pack of Chevy Volt in "T" configuration (left, courtesy of evauthority.com), and battery pack of Tesla Model S with "Floor" architecture (right, courtesy of evworld.com).

Tesla Model S, SmartBatt prototype vehicle and many smaller experimental cars.

To the best of authors' knowledge, no work has been reported in the open literature on predicting damage to the battery pack due to the ground impact. The industry and responsible government agents have not developed yet any safety standards in this regard. Therefore, the degree of protection was left to the discretion of the manufacturers of electric vehicles.

The objective of the present paper is to develop a general methodology of predicting a sequence of local indentation followed by piercing and fracture of the bottom structure of a typical battery pack. The analysis goes further by showing how the individual cells will be pushed from their initial positions, crashed and internally damaged. Based on the previous work of the investigating team [2–5], fracture of the jellyroll, leading to the onset of electric short circuit will also be predicted for some loading cases.

The ground impact is an inter-disciplinary problem and cannot be treated alone by the computational methods of crashworthiness engineering. The success of the present approach rests on the vast experience of the investigating team in projectile perforation and ballistics [6,7], ductile fracture [8], optimum design of armor plates [9,10], constitutive modeling [4], and experimental mechanics [11,12].

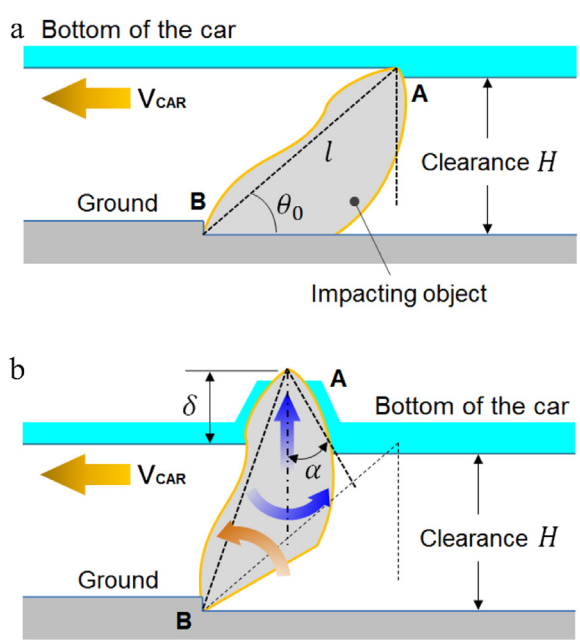

Fig. 2. Schematic of a ground impact scenario: (a) initial state of the irregular-shape object and dominative parameters, and (b) a movement state of the simplified object during impact.

Rather than restricting the analysis to a specific type of a battery pack/vehicle, a more general approach is chosen where a computational model is developed for a battery pack of a generic car. Then, a comprehensive parametric study is performed by changing the material parameters of all individual components as well as the geometry of battery pack. This is possible because modeling of road debris impact is always a local phenomenon. The jellyroll is protected by plastic or metal enclosures of shell casing, module and battery pack housing, and finally components of car body structure. Off all the multiple levels of protection, the most important one is the bottom armor shield, which can be monolithic, sandwich (e.g. SmartBatt) or a combination of the two (e.g. Tesla Model S).

The impact velocity is usually related to the speed of a vehicle. The big unknown is always the shape of the intruding object, which could be sharp and pointed, or blunt such as a towing shank. Therefore, simulations are performed for a practical range of all the above mentioned input parameters. It is found that the critical penetration depth causing the bottom shield to rupture depends on the tip radius of the foreign impacting object, the distance of the indentation point to the nearest boundary of the battery module and the exponent of the power-law hardening curve. A closed-form solution is derived under a certain set of assumptions. Numerical simulations run in parallel remove the restrictive character of some of the assumptions and introduce into the analysis several new input parameters. Once the main armor shield is perforated, other thinner layers of the integrated battery pack will fracture soon after, exposing the lithium-ion cells to direct contact with the road debris or sharp edges of the ruptured armor plate.

A relatively coarse mesh is used in numerical simulation for the global model. In the second stage of the analysis a much more refined models of the cell is introduced to predict what happens next to the jellyroll and at which point the separator fails leading to electric short circuit. Similarly, the shell casing is discretized by very small shell elements to predict possible fracture of the cylindrical part and/or end caps.

A precise characterization of material properties of all the constituents of the battery pack goes beyond the scope of the present paper. The flow and fracture properties of the jellyroll are taken from previous publications of the present authors [2–5]. Very detailed characterization of plasticity and fracture of the steel shell casing is a subject of a separate publication [13]. The properties of steel or aluminum sheets of a car, aluminum extrusion and other plastic parts are taken from a vast data bank of the Impact and Crashworthiness Lab at MIT and the Automobile Crash Lab at Tsinghua University.

The reconstruction of the road debris impact on the bottom structure of electric vehicle from the point of view of electric short circuit, thermal runaway and fire has been a perfect case study to demonstrate what we know and what still should be learned about the predictive computational tools for analyzing safety of lithium-

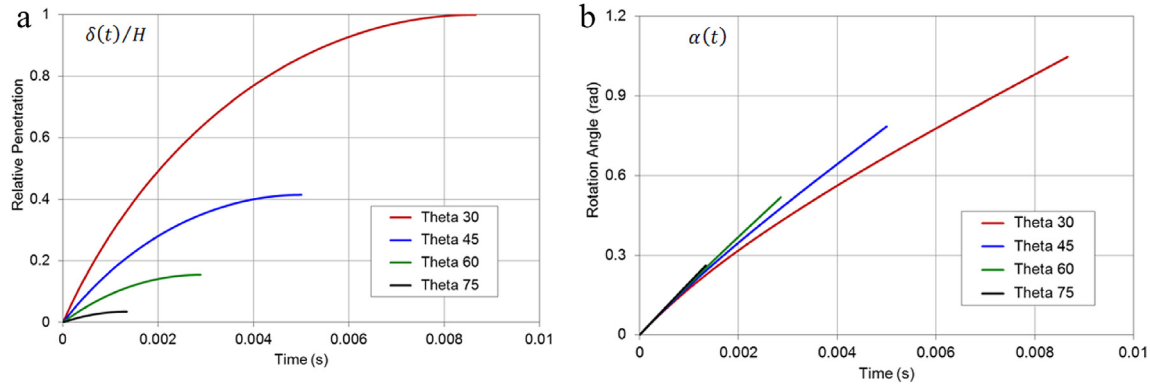

Fig. 3. Histories of vertical displacement and rotation of the impacting object, according to Eqs. (2) and (3).

ion batteries. The present paper brings an important question about the optimum design of individual cells, modules, packs and the integration architecture for maximum possible protection against ground impact. Even though it does not provide all the answers, it offers powerful new computational tools and indicates directions of needed research.

2. Defining ground impact: quasi-static indentation and dynamic impact

The characterization of the road debris and definition of the impact scenario are some of the most difficult parts of the stated research. There are infinite types and shapes of an obstacle and a right choice must be made on the geometry and impact velocity to represent a real-world accident. One input parameter, which is kept constant throughout the rest of the derivation and simulation is the ground clearance H of the vehicle. The other parameter is the characteristic length l of the solid object on the ground. If the size of the object is $l < H$, the ground debris will clear under the car. If, on the other hand $l \gg H$, the car will experience a frontal impact into the bumper or fairing under it.

Besides the length parameter, it is convenient to introduce the angle θ_0 (see Fig. 2a)

$$\sin\theta_0 = H/l \tag{1}$$

We assume the characteristic length is $H < l < 2H$. To have contact with bottom of the vehicle, the range of the angle θ_0 is $30^\circ < \theta_0 < 90^\circ$.

There are at least three different mechanisms through which an object can hit the bottom of the car. One such mechanism is explained in Fig. 2. Because of irregularity of the road surface, the heave and pitch motion of the car and some irregular features of the bottom structure, both extreme ends of the road obstacle could be caught, forming a one degree-of-freedom mechanism. The top end of the object, shown as point A, contacts the bottom of the car and moves together with the car with a speed (V_{CAR}). Meanwhile, the bottom end B of the object remains stuck on the ground, and the object starts rotating around point B and penetrating into the bottom plate of the car. It is assumed that speed of the car does not change due to impact and remains constant.

Three parameters determine kinematics of the object in such an impact scenario: H, V_{CAR}, and the initial angle between AB line and the ground, θ_0. From a simple kinematics of the problem shown in Fig. 2b, the motion of the object around point B can be separated into a vertical indentation $\delta(t)$ and a rotation $\alpha(t)$ in the reference configuration of the car, following Eqs. (2) and (3).

$$\delta(t)/H = \left[(\sin\theta_0)^{-2} - (\cot\theta_0 - V_{CAR}t/H)^2\right]^{0.5} - 1 \tag{2}$$

$$\alpha(t) = \sin^{-1}[(\delta(t)/H + 1)\sin\theta_0] - \theta_0 \tag{3}$$

Indentation of the object achieves maximum when α equals to $90^\circ - \theta_0$. Assuming a most likely speed of car on highways $V_{CAR} = 30\ \mathrm{m\ s^{-1}}$ (67.5 mph), and four different initial inclined angles (30°, 45°, 60° and 75°), histories of the vertical displacement and the rotation angle are plotted in Fig. 3. Note that, except for the specially declared, only the vertical indentation is considered for the ground impact for the simulations presented in this paper.

Another more likely mechanism of the initiation of the indentation process is that the object is stuck between the ground and bottom structure by friction. This is similar to the locking of a drawer if pushed off center. The critical locking angle θ_{cr} depends on the friction coefficient μ. Assuming similar coefficient of friction

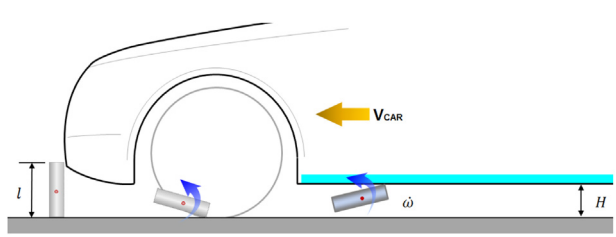

Fig. 4. Schematic of flying object impact against bottom structure of the car.

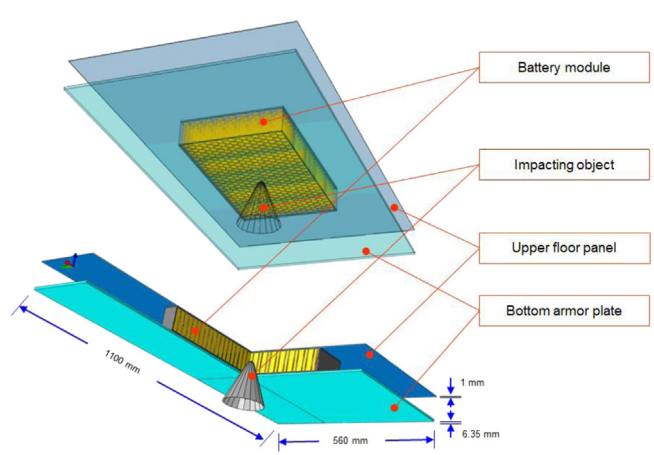

Fig. 5. Composition of the proposed model of integrated battery pack.

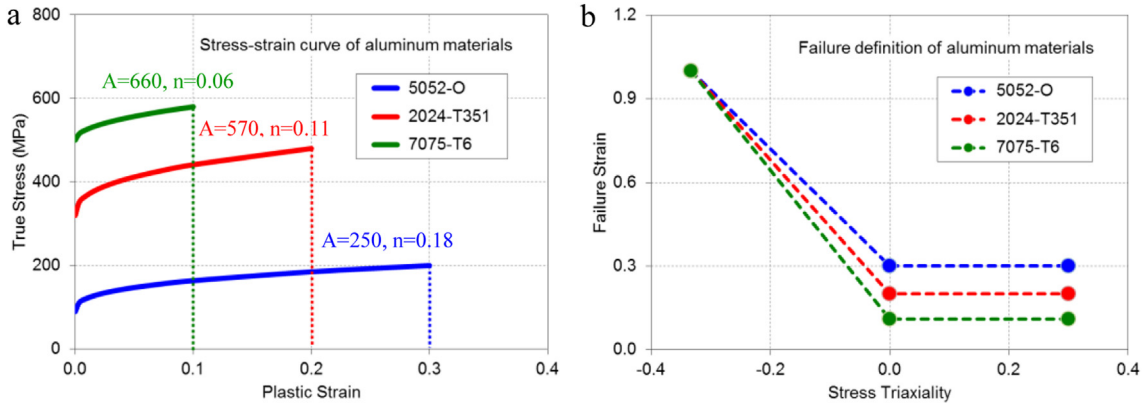

Fig. 6. Material properties of the three grades of aluminum alloys.

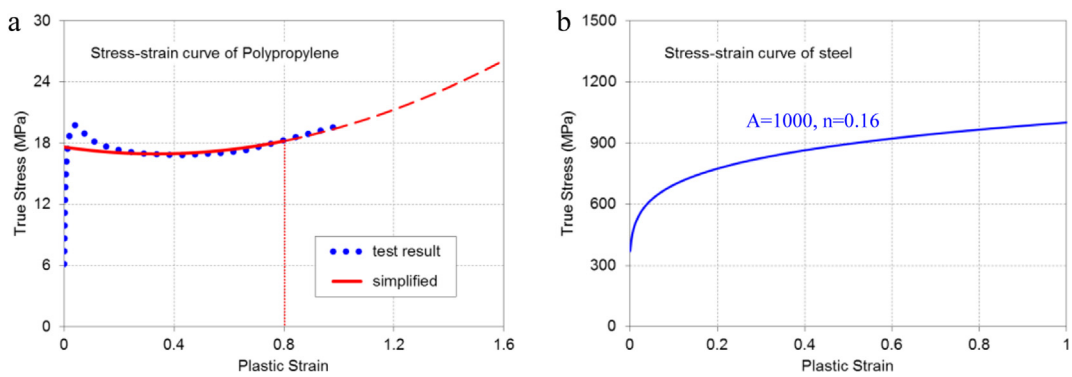

Fig. 7. Material properties of (a) the module housing and (b) the shell casing.

between the object with the road or vehicle, the critical angle to lock is:

$$\tan\theta_{cr} = 1/\mu \tag{4}$$

From the geometry of the problem, the maximum relative penetration is

$$\delta_{\max}/H = 1/\sin\theta_{cr} - 1 \tag{5}$$

Eliminating the parameter θ_{cr} between Eqs. (4) and (5) gives the expression for the maximum relative penetration in terms of the friction coefficient

$$\delta_{\max}/H = \sqrt{1+\mu^2} - 1 \cong \frac{1}{2}\mu^2 \tag{6}$$

For example, taking $\mu = 0.3$, and $H = 0.15$ m, the maximum penetration will be $\delta_{\max} = 6.8$ mm. In the case of $\mu = 0$, i.e. no friction existing between the object and the bottom structure (or the ground), there is no penetration. The case of $\mu = 1$ corresponds to another extreme case where $\delta_{\max}/H = \sqrt{2} - 1$ and $\theta_{cr} = 45°$.

The third impact mechanism is when a taller obstacle ($l > H$) hit by the front of the car, it acquires an initial angular velocity, causing the road debris to tumble under the car and in this process hitting the bottom structure. The above scenario involves many additional parameters but indicates that the object could take off from the ground and rotate around its center of gravity, see Fig. 4. This case of dynamic impact is considered in the present simulation by eliminating the rotation effect where the mass of the impacting object is an additional parameter.

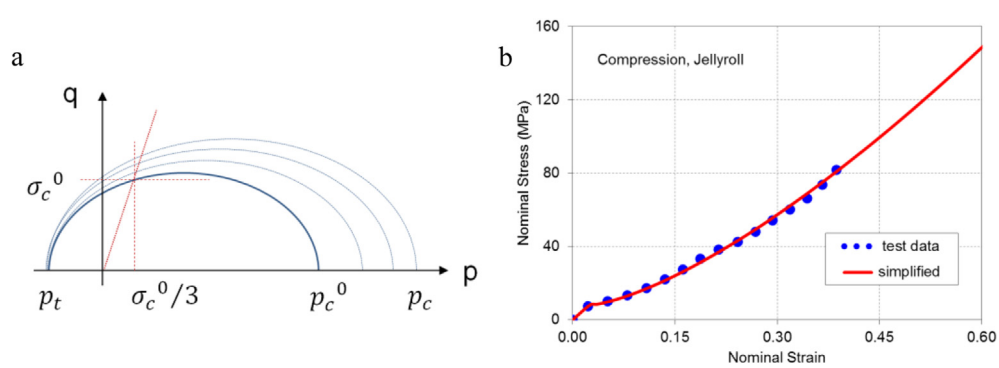

Fig. 8. Homogenized material model and properties of the jellyroll.

Finally, it is recognized that the failure sequence also depends on the tip geometry of the road debris. Two-parameter representation is used with the tip radius R_b and the cone angle β, see Fig. 22.

3. Characterization of mechanical and fracture properties of components in the integrated battery pack

The hypothetical model of the integrated battery pack proposed in the present paper consists of five to six components: (i) shell casing, (ii) jellyroll of individual battery cells, (iii) battery module housing, (iv) armor shield plate, (v) floor panel, and/or (vi) cross member for additional reinforcement. Fig. 5 provides a transparent isometric view and a cut view of such an assembly (without the cross member). The impacting mass with a cone shape and a tip radius is also included in Fig. 5.

It is assumed that the major relevant structural components of the car body, such as armor plate, floor panel, and cross member, adopt the same type of aluminum alloy. To study the influence of material properties of the car body on impact results, three grades of aluminum alloy, 2024-T351, 5052-O and 7075-T6, are considered [14]. Fig. 6a shows the equivalent stress–strain curves of the three grades of aluminum alloy, where 5052-O presents the highest ductility and lowest strength, while 7075-T6 presents the lowest ductility and highest strength. The isotropic von Mises model is used to characterize the plasticity of the aluminum alloys. Ductile damage model and element removal technique in ABAQUS/Explicit are chosen to model fracture initiation and propagation. A simplified failure criterion is defined for each of the aluminum alloy materials, as shown in Fig. 6b, which distinguishes the difference of failure strains between compression and tension stress states, but disregards the variation of failure strain within the range of positive stress triaxiality. The constant failure strain for positive stress triaxiality is taken to be the plane strain fracture. This is the worst case state, the uniaxial and equi-biaxial failure strain should be much higher [8,12].

The battery module housing could be manufactured with lightweight metallic material (e.g. aluminum) or nonmetallic material (e.g. injection molded plastic). Here the properties of a generic thermoplastic material for car interiors are selected to model the module housing, as shown in Fig. 7a. A similar ductile damage model is defined for module housing material while the fracture strain values are much larger than those of aluminum alloys [15,16].

To achieve an acceptable computational efficiency with the global model of battery pack, the components in individual battery cells, i.e. the shell casing and the jellyroll, are greatly simplified. Accordingly, the homogenized characterization of their mechanical behavior is applied, and no fracture behavior is defined for the battery cells at the global model level. Failure of the jellyroll is studied in a separate section using a detailed model of the cell. Based on the experimental study on battery cell components in the authors' laboratories, the elasto-plastic properties of a type of high-strength steel and the isotropic von Mises model are selected to characterize the shell casing, as shown in Fig. 7b.

The jellyroll inside the shell casing is characterized by volumetric compressibility during compression and abrupt ascendance of reaction force at a large compression stage, close to behaviors of some metal foam materials. A pressure-dependent crushable foam model in ABAQUS [17] is selected to characterize the homogenized properties of jellyroll. The crushable foam model is an extension of the one developed by Deshpande and Fleck in Ref. [18]. Besides the original feature of isotropic hardening law in the Deshpande and Fleck model, it incorporates a new option of a volumetric hardening law and the corresponding yield function to address the transition from hydrostatic compression to tension (see Fig. 8a), which is more suitable for describing the mechanical behavior of the jellyroll [4,5]. The yield function has the form

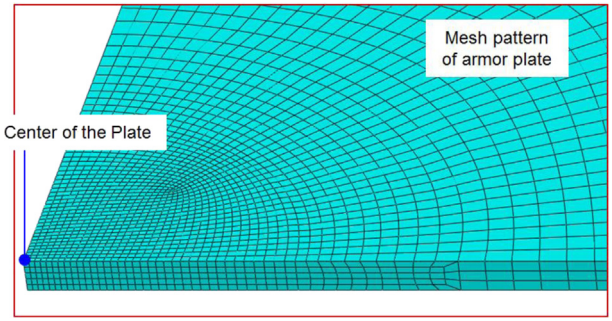

Fig. 9. Mesh of the armor plate.

$$F \equiv \sqrt{q^2 + \alpha^2 \left(p - \frac{p_c - p_t}{2}\right)^2} - \alpha \frac{p_c + p_t}{2} \tag{7}$$

where p is the pressure, q is the Mises stress, p_c and p_t are the hydrostatic compression and tension yield strengths, respectively. $\alpha = 3k/\sqrt{(3k_t + k)(3 - k)}$ is the shape factor of the yield surface, where $k = \sigma_c^0/p_c^0$, $k_t = p_t/p_c^0$, and σ_c^0 and p_c^0 are the initial yield strengths in uniaxial compression and hydrostatic compression, respectively.

In the present paper, $\sigma_c^0 = 8$ MPa, which is directly extracted from the longitudinal-direction compression tests of the pouched battery cells performed in the authors' laboratory (see Fig. 8b and Ref. [5]). As shown with the "simplified" curve in Fig. 8b, the segment before the data point of σ_c^0 is used to estimate elastic modulus of the jellyroll material, while the remaining segment is converted into true stress vs. true plastic strain and input as hardening law in the crushable foam model. Based on experimental observation, it is also reasonable to assume prominent compressibility for the jellyroll material. Thereby value 1.1 is assigned to k, referring to test data of a foam material in Ref. [19], which means the uniaxial and hydrostatic compression yield strengths are close to one another. Also considering that unloading behavior or tension is not the dominant stress state in the present study, value 0.1 is assigned to k_t, which implies a small value of tensile cut-off.

To properly characterize both the yield behavior and the plastic deformation, a non-associate flow rule is adopted with a flow potential G

$$G = \sqrt{q^2 + \frac{9}{2}p^2} \tag{8}$$

where the coefficient 9/2 indicates that the plastic Poisson's ratio is zero for the material.

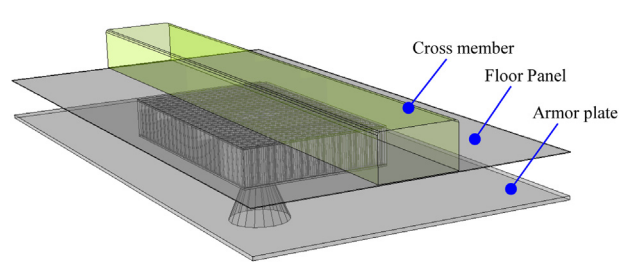

Fig. 10. A model including the cross member.

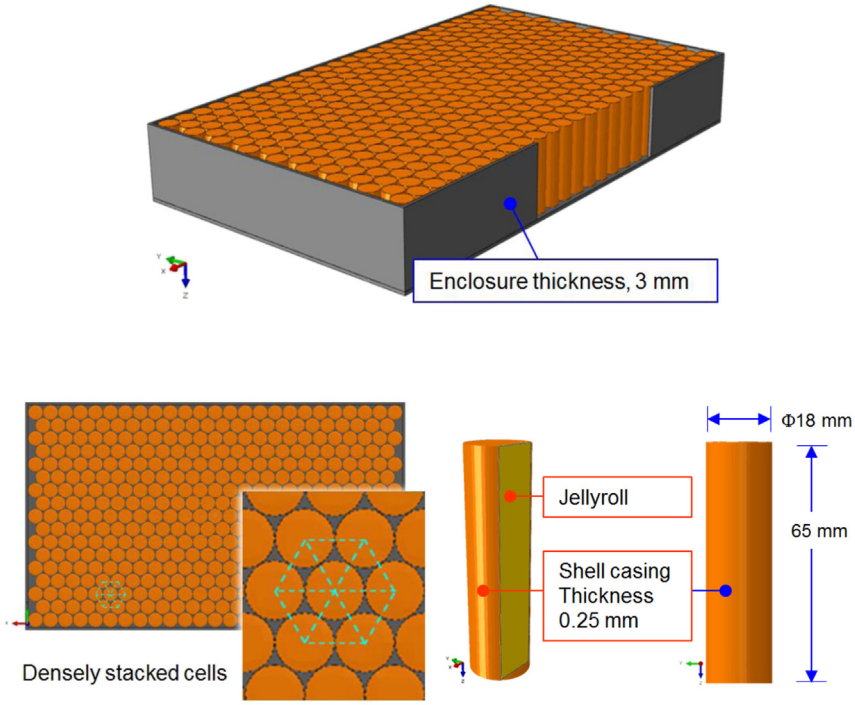

Fig. 11. Battery module, the compact layout of battery cells and dimension of battery cell.

4. Modeling of vehicle body structure: armor plate, cross members and floor panel

In the simplified battery pack model, the armor plate is an aluminum plate with the initial thickness h_0. The magnitude of h_0 can be easily changed in the simulation but in most calculations the value $h_0 = 6.35$ mm (1/4 inch) is assumed. The plate is large and spans about one third of longitudinal and transversal dimension of a typical car, respectively. As a fairly thick plate, it is discretized with solid elements. In the middle area where deformation is mainly concentrated during the process of indentation, a fine mesh is adopted with the characteristic element length of 1 mm, as shown in Fig. 9. The floor panel is simplified as a thin aluminum plate with the thickness of 1 mm.

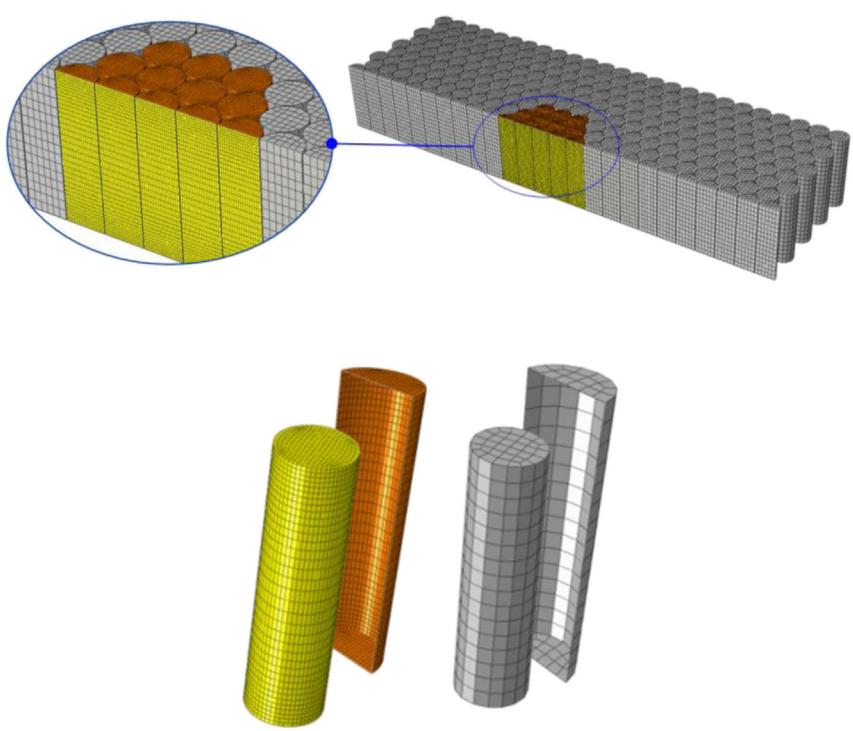

Fig. 12. Mesh of the battery cells.

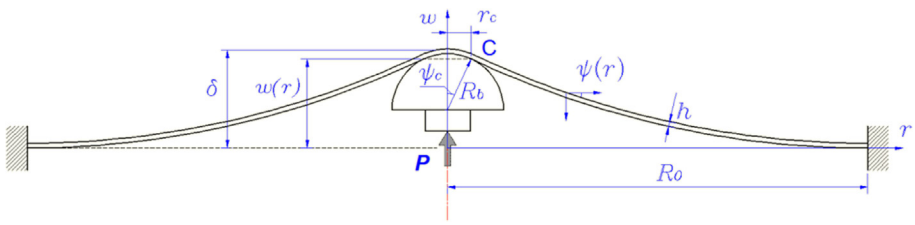

Fig. 13. Geometry of a clamped thin plate loaded quasi-statically by a hemispherical punch.

In reality, the road debris could impact against a position of the bottom structure where a cross member could be installed above the floor panel for the purpose of reinforcement. To compare the situations with and without the additional reinforcement, an extruded aluminum box beam with square cross-section is added upon the floor panel plate in one of the simulations, as shown in Fig. 10. Both the armor plate and the floor panel in the simplified model are clamped at the four sides. For the model with additional cross member, the two ends of the cross member are fully fixed.

5. Modeling of battery module: plastic enclosures and cells

Considering the localized character of the ground impact, only one battery module 456 × 274 mm in size is assumed to be involved. Enclosure of this module is constructed with plastic plates 3 mm thick, also discretized with solid elements. In the simplified model, the battery module is embedded between the armor plate and the floor panel, forming a sandwich-like structure.

More than 400 battery cells are vertically oriented and stacked inside the plastic enclosure of the module with a compact layout, as shown in Fig. 11. Each individual cell directly contacts six neighboring cells (except for the ones at the most outer side of the stack), while connection tabs and cooling systems existing in a realistic battery module are not included in the current model.

Batteries inside the pack are standard 18650 lithium-ion cells with a height of 65 mm and diameter of 18 mm. For each battery cell, the jellyroll is wrapped by a very thin shell casing. Taking an average thickness of 0.25 mm [4,13], the shell casing is modeled with shell elements. A much finer solid element mesh is introduced in the next sections to model the fracture of shell casing. The homogenized jellyroll is modeled with solid elements. Fig. 12 shows the mesh pattern of the battery cells. The cells in the impacted area are finely meshed and a much coarse mesh is used to model remaining cells.

6. Analytical solution (closed-form solution)

Analytical solutions provide a quick estimate on displacements and strains and identify a group of parameters controlling a response of a given structure. The ground impact is modeled here as a local indentation of a clamped circular plate by a hemispherical punch of a radius R_b. The solution is carried out all the way to failure and involves large deflections for which membrane action is the dominant load-resisting mechanism. The resulting plastic deformations are large and therefore elastic strains are disregarded. It is assumed that the armor shield material obeys the power hardening law defined by the amplitude A and the exponent n, according to

$$\overline{\sigma} = A\overline{\varepsilon}^n \tag{9}$$

All geometrical parameters are defined in Fig. 13. The outer radius of the circular disc R_0 represents a distance of the impact point to the nearest boundary of the affected module. The initial thickness of the armor plate is denoted by h_0 and this is one of the main parameters in the solution. In the cylindrical coordinate system r denotes the radius of the plate, and the current displacement and slope of the deflection line are denoted respectively by $w(r)$ and

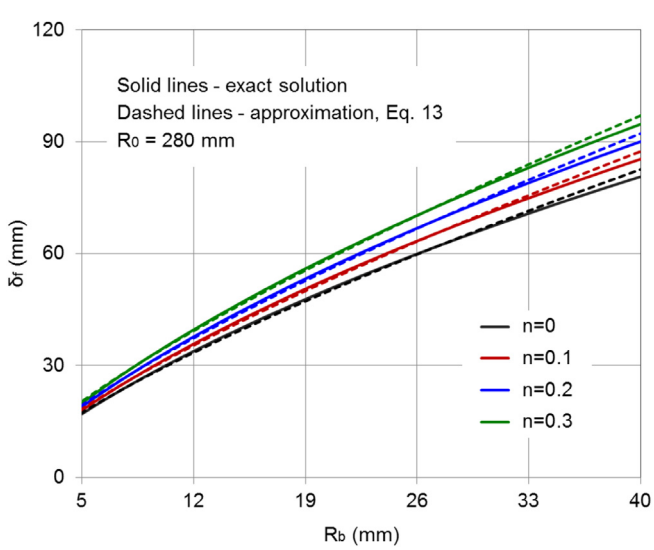

Fig. 14. Relationship between the displacement at failure and the radii ratio for different material hardening exponents.

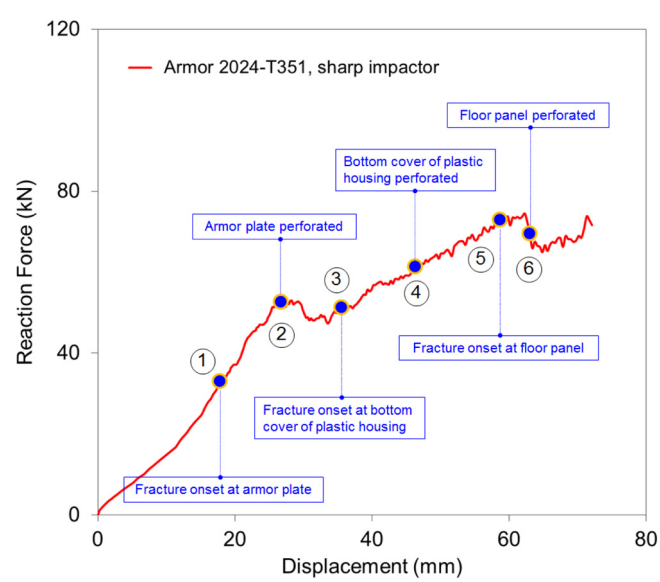

Fig. 15. Force-displacement of the reference case and moments of fracture onset or perforation at different components.

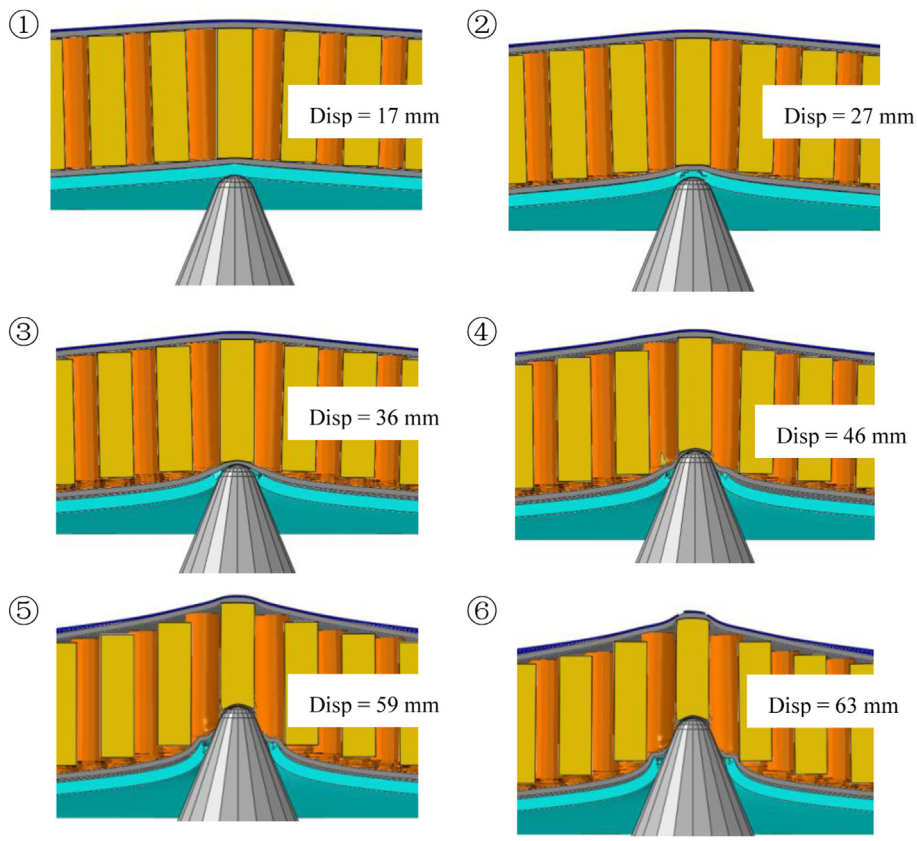

Fig. 16. The simulated indentation process of a punching object into the battery pack.

$\psi(r)$. In the quasi-static solution, the process parameter is the displacement of the punch (indentation depth) δ or the coordinates of the inflection point C, $r_c = R_b \sin \psi_c$. In the case of dynamic loading, the process parameter is time.

A complete closed-form solution of this problem was derived by Simonsen and Lauridsen [20] and in a slightly modified form by Lee et al. [10]. Only the final results are quoted here. The relationship between the total resisting force P and the displacement of the punch δ, is given in the parametric form

$$\frac{\delta}{R_b} = 1 - \cos \psi_c + \sin^2 \psi_c \ln \left[\frac{R_0/R_b + \sqrt{(R_0/R_b)^2 - \sin^4 \psi_c}}{\sin \psi_c (1 + \cos \psi_c)} \right] \tag{10}$$

$$P = 2\pi A h_0 R_b [-\ln \cos \psi_c]^n \cos \psi_c \sin^2 \psi_c \tag{11}$$

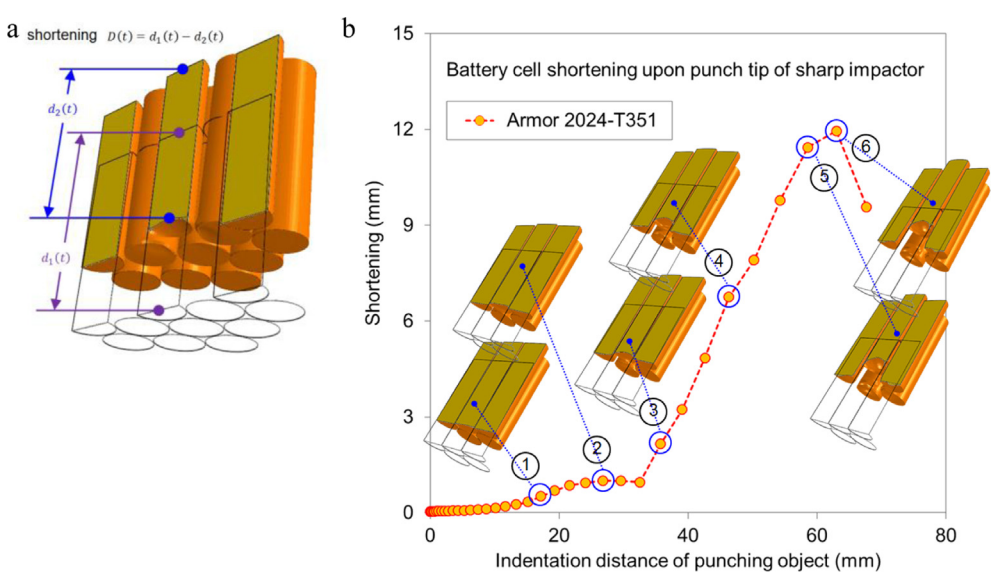

Fig. 17. Battery cell shortening during the indentation of the punch tip against the battery pack assembly.

where the inflection point of the deflection line ψ_c is the process parameter. Note that Eq. (10) follows an assumption of rigid-plastic material; otherwise it is difficult to derive the exact analytical expression of δ with the power hardening law of material. The reader is referred to the above papers for details of the derivation and justification of additional simplifying assumptions. The analytical solutions were also compared with numerical simulation of the same problem and experimental data on circular, square and rectangular plates.

The closed-form solution goes further and can predict the failure of the plate either by stability analysis [20] or fracture analysis [10]. According to the stability criterion, the load-carrying capacity of the plate is exhausted when the resisting force reaches maximum and the inflection wrapping angle ψ_c (inflection point in Fig. 13) reaches a critical value

$$\psi_{cr} = 0.957 + 0.4n \tag{12}$$

Substituting the above expression into Eqs. (10) and (11), one can calculate the maximum force at failure, P_f and the punch displacement to failure, δ_f. The relationship of the displacement to failure δ_f in terms of punch radius R_b for four representative values of the exponent n and a fixed value of plate radius $R_0 = 280$ mm is plotted in Fig. 14 as solid lines.

A good power fit of the exact solution (Eqs. (10) and (11)) is given by the following expressions which could be conveniently used in practical application.

$$\delta_f = 1.27(1 + 0.58n)R_b^{3/4}R_0^{1/4} \tag{13}$$

$$P_f \Big/ (2\pi A h_0 R_b) = 0.077(5 - 3n) \tag{14}$$

Approximations based on Eq. (13) are plotted in Fig. 14 as dashed lines. It should be recalled that these equations are applicable for deflections larger than the plate thickness, for which membrane assumption is justifiable. It is interesting to note that the amount of penetration causing fracture of the armor plate is then independent on the thickness of the armor plate. Also, there is a relatively weak dependence of δ_f on the hardening exponent n and the plate radius R_0. Under a sharp tip of the road debris, fracture occurs very early in the deformation process.

After the onset of fracture, radial cracks are propagating from the initial opening. The analysis of this stage was given by Wierzbicki [21] and Lee and Wierzbicki [22], where also the dynamic solution was presented. However in the present problem after fracture occurs in the armor plate, other components in the battery pack are inevitably involved into the penetration process and their influence on the global and local response cannot be neglected, which will be shown in Section 7.

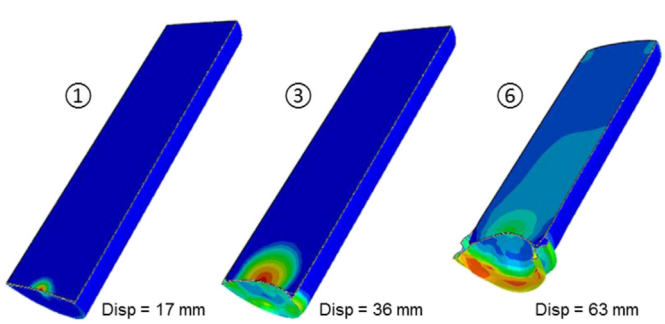

Fig. 18. Plastic strain distribution in central battery cell during indentation of the punch tip.

Table 1
Summary of the FE models used for parametric study.

Case no.	0[a]	1	2	3	4	5	6
Body material	2024-T351	5052-O	7075-T6	2024-T351			
Armor thickness (mm)	6.35			3.17	6.35		
Punch tip shape	Sharp				Blunt	Sharp	
Cross member	No					Yes	No
Loading condition	Quasi-static						Dynamic

[a] Case 0 is the reference case.

7. Results of global numerical simulation of the battery pack

7.1. Reference case

As a reference case the armor plate was taken to be made from aluminum alloy 2024-T351, additional reinforcement of cross member was disregarded, and the integrated battery pack was quasi-statically punched by the impacting object with a small radius punch tip. The impacting object was simplified as a cone-shaped analytical rigid body in ABAQUS. The tip radius is $R_b = 10$ mm and the semi-apex angle is 45° for the sharp impacting object, compared to a blunt one in another case with the tip radius of $R_b = 20$ mm and the semi-apex angle of 90°.

Fig. 15 shows the force-displacement curve extracted from the simulation. The points marked as ①–⑥ on the force-displacement curve define the sequence of the fracture process in different components of the battery pack assembly. The armor plate, the bottom cover of the plastic housing and the floor panel fracture sequentially, while no fracture was observed for the upper cover of the plastic housing. The first peak of the force-displacement curve appears when the armor plate is just perforated. The bottom cover of the plastic housing fractures under the subsequent push by the punch tip and along with the radial cracks propagating around of the perforated hole in the armor plate, while the resistance against the punch tip (presented with the average slope of a segment in the

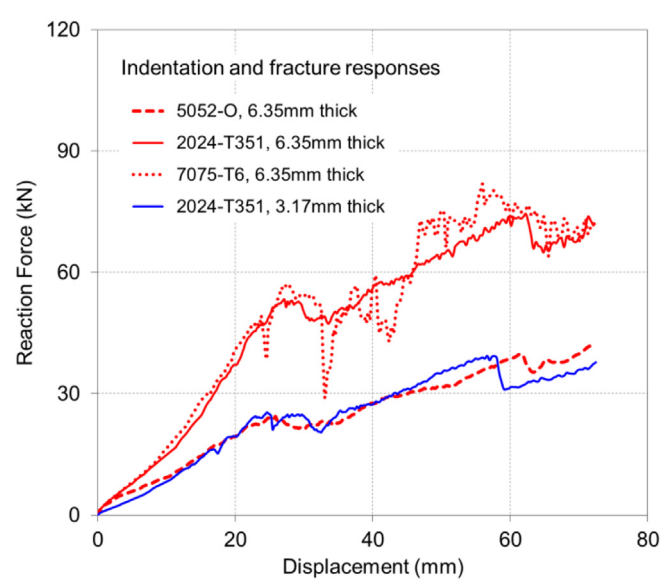

Fig. 19. Force-displacement responses for indentation against battery packs with different body materials or armor plate thickness values.

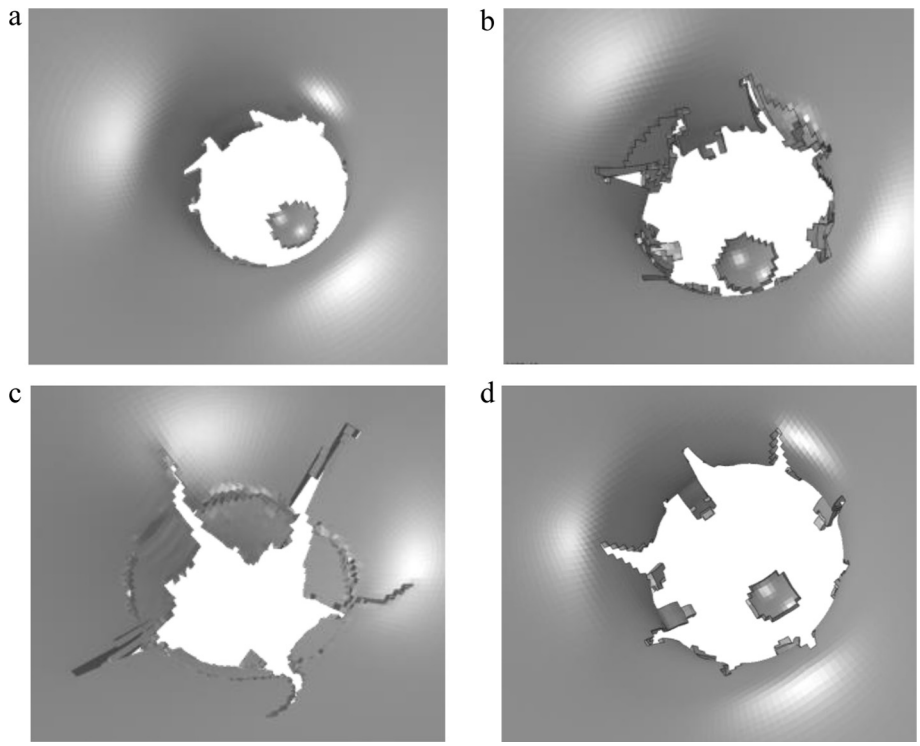

Fig. 20. Fracture pattern of the armor plate after punching in the three cases of Study 1 with different combinations of body material and armor plate thickness: (a) 5052-O and 6.35 mm (Case 1), (b) 2024-T351 and 6.35 mm (Case 0), (c) 7075-T6 and 6.35 mm (Case 2), and (d) 2024-T351 and 3.17 mm (Case 3).

curve) drops by some 20%. When the floor panel is perforated at the later stage, another force drop is observed.

The indentation displacement of the punching tip at the first force peak is about 27 mm. Recalling Eq. (13) and $n = 0.11$ for aluminum material 2024-T351, $R_b = 10$, $R_0 = 280$ (half of the shorter-edge length for the armor plate in simulation), the membrane-theory solution of the failure displacement is 31 mm, which is quite close to the exact numerical solution.

Fig. 16 exhibits a sequence of deformation and failure with a side cut view of the whole assembly of the battery pack in the reference case, with each frame corresponding to a marked number in Fig. 15. During the indentation process, fracture of the armor plate in the punched area occurred first. Crack propagation in the armor plate goes through circumferentially around the punch tip, leaving a cap on the punch tip and a hole in the armor plate. Further indentation of the punching object enlarges the diameter of the punctured hole and deforms the plastic enclosure of the battery module. Deformation becomes more concentrated in the area exactly above the punch tip, leading to propagation of radial cracks in the plastic plate. The individual battery cells above the punching tip are pushed upward during the indentation process. Before fracture of the armor plate, deflection of the armor plate covers a relatively large area, the punching load is transmitted more evenly over the armor plate, and a relatively large number of cells are affected in terms of their upward motion. After the armor plate is punctured, deflection of the armor plate becomes more concentrated around the edge of the punctured hole, and fewer individual cells are continuously pushed upward. At the

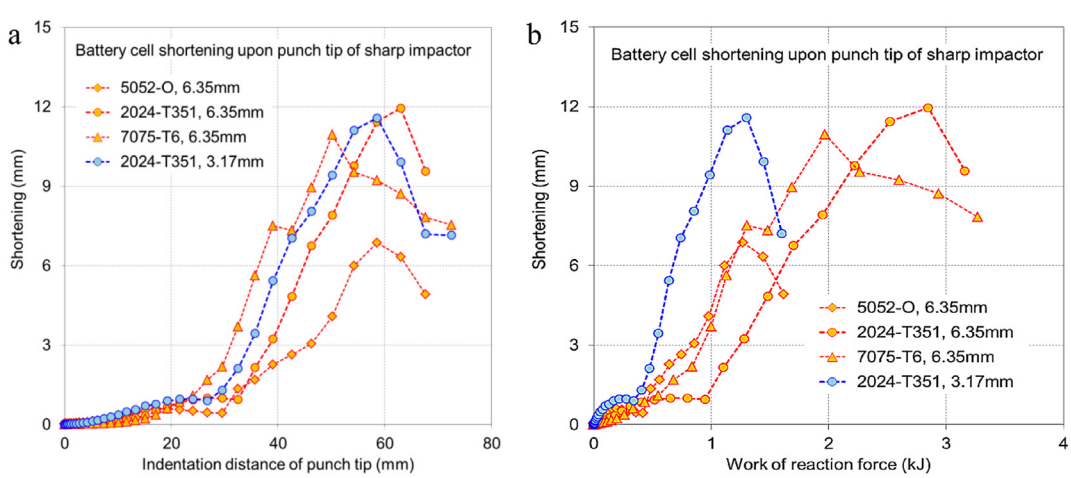

Fig. 21. Battery shortening in battery packs with different body materials or armor plate thickness values.

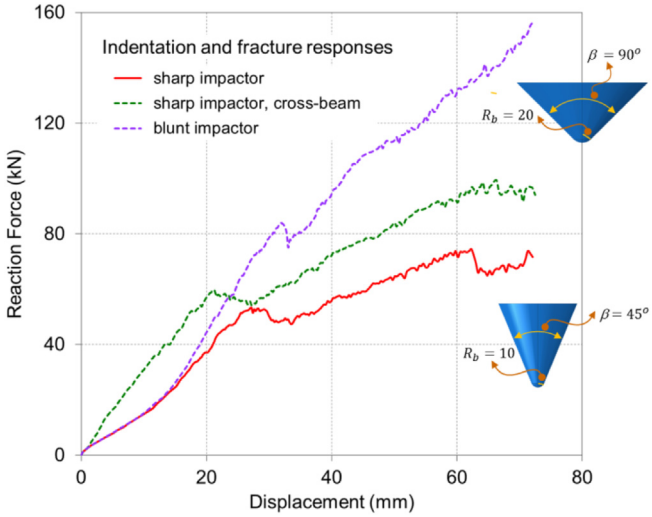

Fig. 22. Force-displacement responses for indentation against battery packs in the three cases of Study 2 and Study 3.

same time, the upward moved cells push against the floor panel. In other words, the floor panel provides a secondary indentation resistance mechanism. The gradually concentrated indentation from the punch tip and the resistance from the floor panel cause compression and shortening of the cells exactly above the punching tip. It can also be noticed from the last frame in Fig. 16, that the upward moved battery cell finally punctured the floor panel. At the stage of the global model, the battery cell failure is not included in the modeling. A detailed model of the jellyroll and shell casing is presented in Sections 8 and 9.

Shortening of the battery cells above the punch tip vs. the indentation distance of the punch is shown in Fig. 17, in which three different stages of the battery cell deformation can be more clearly distinguished. At the first stage, the battery is shortened slightly. Once the armor is perforated, an apparent turning point is observed on the curve, and the battery starts to be dramatically shortened within a small indentation distance. Along with the global shortening in height of the battery cell, the local buckling/folding at the lower end of the shell casing emerges and the local plastic deformation of the jellyroll becomes severely concentrated at the punched point, as shown in Fig. 18. Both of the two locations correspond to potential failure of the central battery cell. As the indentation process continues, the floor panel is punctured, resistance to the upward motion of battery cells is partially released and the battery cell above the punch tip is unloaded. This corresponds to the third stage of the battery shortening, where elastic deformation of the battery is recovered.

In reality, the maximum amount of penetration possibly achieved in the ground impact depends on the geometry of the road debris and its interaction with the frontal or/and bottom part of the vehicle body, as described in Section 2.

To investigate the influence of the inherent features of the battery pack assembly (e.g. material and geometrical parameters) as well as the external factors (e.g. the shape of impacting punch tip and the loading condition) on the indentation resistance of the structure and the local shortening extent of individual battery cells, a series of parametric study are carried out by varying different model parameters. A summary of all the models is shown in Table 1.

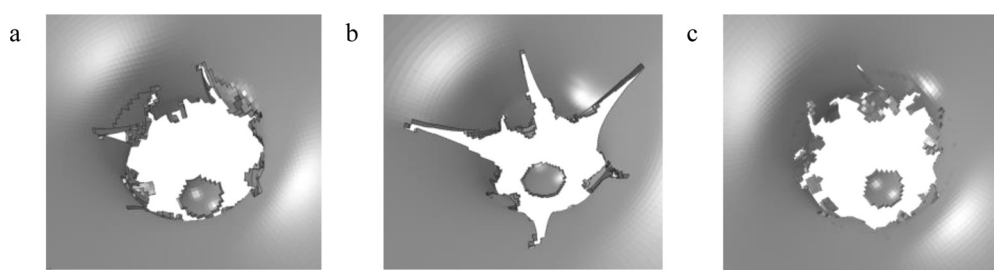

Fig. 23. Fracture pattern of the armor plate after punching in the three cases of Study 2 and Study 3: (a) sharp punch tip (Case 0), (b) blunt punch tip (Case 4), and (c) sharp punch tip and cross member (Case 5).

Fig. 24. Battery shortening in battery packs in the three cases of Study 2 and Study 3.

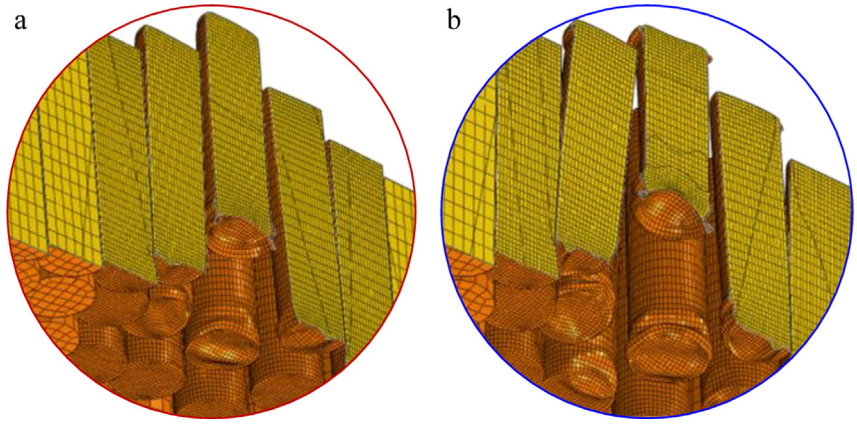

Fig. 25. Final state of battery cell shortening in the cases of Study 3: (a) without cross member (Case 0), and (b) with cross member (Case 5).

7.2. Study 1: Influence of body structure material and armor plate thickness

A comparison of the response of three grades of aluminum in terms of the load–displacement response is shown in Fig. 19. The reference case takes aluminum 2024-T351. The assembly with lower-strength and high-ductility body material (aluminum 5052-O) presents apparently lower indentation resistance, while the assembly with high-strength and low-ductility body material (aluminum 7075-T6) presents a little higher indentation resistance before the armor plate is perforated. It reflects a strong dependence of the indentation resistance of the battery pack assembly on the average strength of the body material. The indentation distances corresponding to armor plate perforation in the three cases are close to each other, showing weak dependence of the failure displacement on the average strength of the body material as predicted by the analytical solution.

By observing the final fracture patterns in these three cases (Fig. 20a–c), one can also distinguish another effect of using different body materials. In the armor plate of ductile material 5052-O, the circumferential crack with smaller radial cracks is formed while with the reduced ductility of material (e.g. using 2024-T351 and 7075-T6), larger radial cracks are generated from the edge of circumferential crack. In the armor plate of material 7075-T6, the intensively developed radial cracks even form sharp slant edges like knives that become more dangerous to the plastic housing of battery module and the individual battery cells locating at the punch tip.

Shortening of the battery cell above the punch tip exhibits significant difference in the three cases using different body materials, as shown in Fig. 21. Comparing the intensified shortening stage after perforation of the armor plate, from Fig. 21a, it can be seen that, under the same indentation distance of the punch tip, shortening of battery cell increases along with the decrease of material ductility. However, from Fig. 21b, a more practical conclusion can be drawn that, with the same external work, an optimized combination of the strength and ductility of the body material can be found to keep the shortening of battery cell as small as possible, comparing Case 0 to Case 1 and Case 2. Also the extent of the damage to individual battery cells cannot be simply judged from the indentation resistance of the whole assembly.

An additional simulation was performed with a much thinner armor plate of $h_0 = 3.17$ mm. The resisting force is shown to be linearly dependent on the initial plate thickness. At the same time, Fig. 19 proves that the punch penetration to fracture does not depend on the plate thickness. This behavior was predicted exactly by the analytical solution, Eqs. (13) and (14). The above results provide an important clue for optimum design of the bottom armor shield.

7.3. Study 2: Influence of punching tip shape

In Case 4 the battery pack assembly is indented by a blunt punch tip with tip radius of 20 mm and semi-apex angle of 90°, compared to the sharp tip indentation in previous models.

The force-displacement response of Case 4 is obviously higher than that of Case 0, as shown in Fig. 22. According to analytical solution, given the same armor plate material and thickness, the force level before failure is mainly controlled by the punch tip radius. It is well demonstrated by the simulation results at the stage before armor plate perforation. For the further intrusion of the punch tip into the battery pack assembly, the force level is also affected by the semi-apex angle of the punching object. The radial crack under the action of blunt tip exhibits larger length and more apparent extent of propagation, which is closely related to the large semi-apex angle of the blunt punch tip, see Fig. 23a and b. Regarding threats to the individual battery cells, it can be seen that shortening of the battery cell in the central position in the case of blunt punch is much smaller than that in the case of sharp punch, as

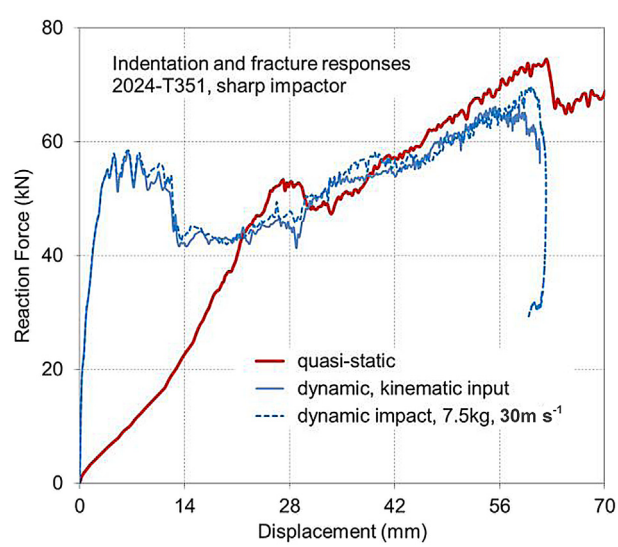

Fig. 26. Force-displacement responses for indentation against battery packs in the quasi-static case and the dynamic cases.

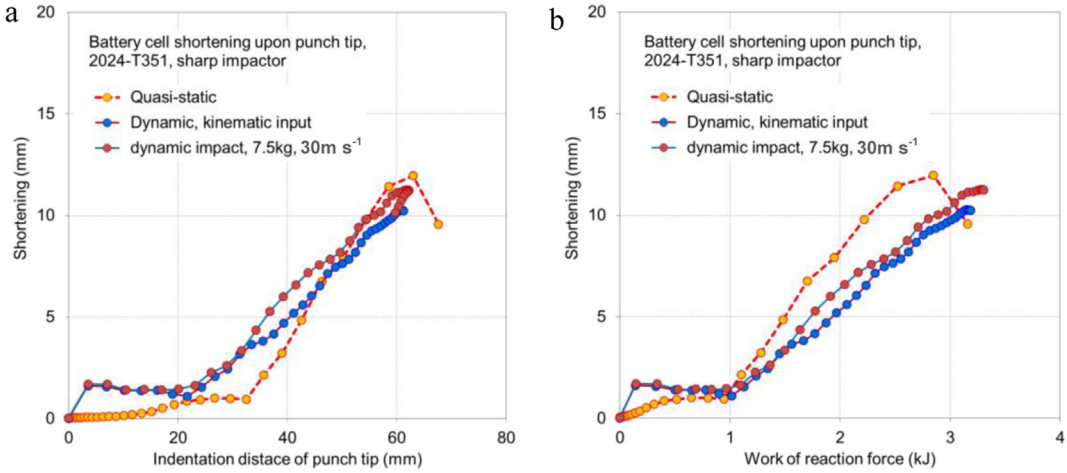

Fig. 27. Battery shortening in battery packs in the quasi-static case and the dynamic cases.

shown in Fig. 24. The explanation is that, during the indentation of blunt tip, a larger portion of the energy is absorbed by the armor plate owing to the large contact area and prominent propagation of radial cracks; at the same time, a relatively large number of the adjacent battery cells are affected and their deformation also shares a part of resisting force.

7.4. Study 3: Influence of cross member (additional reinforcement)

When a cross member is added upon the floor panel as an additional reinforcement to the body structure, the result of ground impact to the battery pack assembly becomes very different. As shown by a green line (in the web version) in Fig. 22, a larger indentation resistance is provided by the reinforced structure in Case 5 compared to that in Case 0. The whole response of the assembly deviates much from the membrane theory solution, which could be described as a problem related to indentation process of a plate with elasto-plastic foundation.

Comparing the fracture patterns of armor plate in Case 0 and Case 5, one can also observe from Fig. 23a and c that the radial cracks growth around the hole punctured in the armor plate in the case with cross member is not so severe as that in the case without such an additional reinforcement. However, the central battery shortening in Case 5 is much greater than that in Case 0 during the initial indentation stage, as shown in Fig. 24, indicating that the possibility of electric short circuit of the battery cells just beneath it is much greater. A close view of the battery cell shortening after punching is exhibited in Fig. 25, where the shell casing buckling at the upper end of individual battery cells at the affected zone can be observed in the case with cross member. This is one of the apparent differences between the two cases in Study 3, implying larger possibility of the battery cell short circuit during indentation against the battery pack assembly.

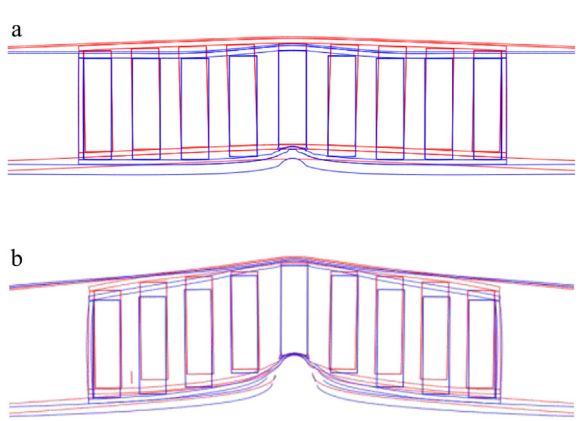

Fig. 28. Comparison between quasi-static and dynamic case: deformation profiles of the battery pack assembly (red line – quasi-static case, and blue line – dynamic case): (a) small punch tip indentation (10 mm), and (b) large punch tip indentation (45 mm). (For interpretation of the references to color in this figure legend, the reader is referred to the web version of this article.)

7.5. Study 4: quasi-static vs. dynamic impact

Three dynamic impact simulations are carried out in this study (Case 6). In the first simulation, a prescribed velocity is defined for the rigid body (the punch tip) following the blue line (in the web version) in Fig. 3a, where the velocity starts from 30 m s^{-1} and gradually ramps down to zero. Here the first simulation is denoted as Case 6-1. In the second simulation (Case 6-2), an impact loading condition is defined for a mass, where the initial velocity is also 30 m s^{-1} and the tip shape of the punching mass is the same as the sharp tip in Case 6-1. The simulations indicate that, with different mass values and the same initial velocity, the force-displacement responses of the dynamic impact cases are identical before rebound, and the mass of road object mainly affects the distance at rebound. It is found that, the distance at rebound in Case 6-2 with a mass of 7.5 kg is very close to the maximum displacement of the punch tip in Case 6-1, as shown in Fig. 26.

Fig. 26 also provides the comparison of the force-displacement between the quasi-static case (Case 0) and the dynamic case (Case 6). Before the armor plate perforation the peak force in the dynamic case is much higher at the same displacement. Therefore, in the dynamic case, perforation of the armor plate occurs relatively early with respect to the indentation distance of the punch tip, also configuring earlier threats to the battery cells. This can be more clearly seen from Fig. 27a, where the shortening of battery cell in dynamic case is more severe than that in quasi-static case for the indentation process from small to intermediate distance.

However, from the point of view of energy, as shown in Fig. 27b, shortening of the central battery cell in the dynamic case becomes smaller than that in the quasi-static case when dissipation of the reaction force work exceeds a relative low value, saying 1 kJ. This can be explained with the deformation profile comparison in Fig. 28. In the dynamic punching process, the armor plate is more locally dented and the punch tip is better wrapped by the affected area. After perforation of the armor plate the early-formed local curvature produces larger resistance to the punching tip. In the

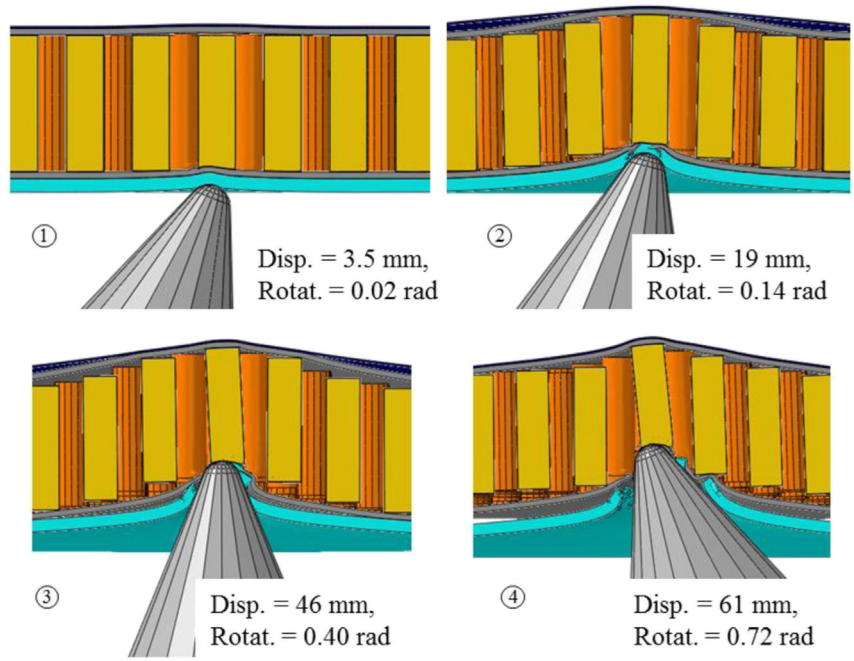

Fig. 29. Indentation process of a punch tip with rotation into the battery pack.

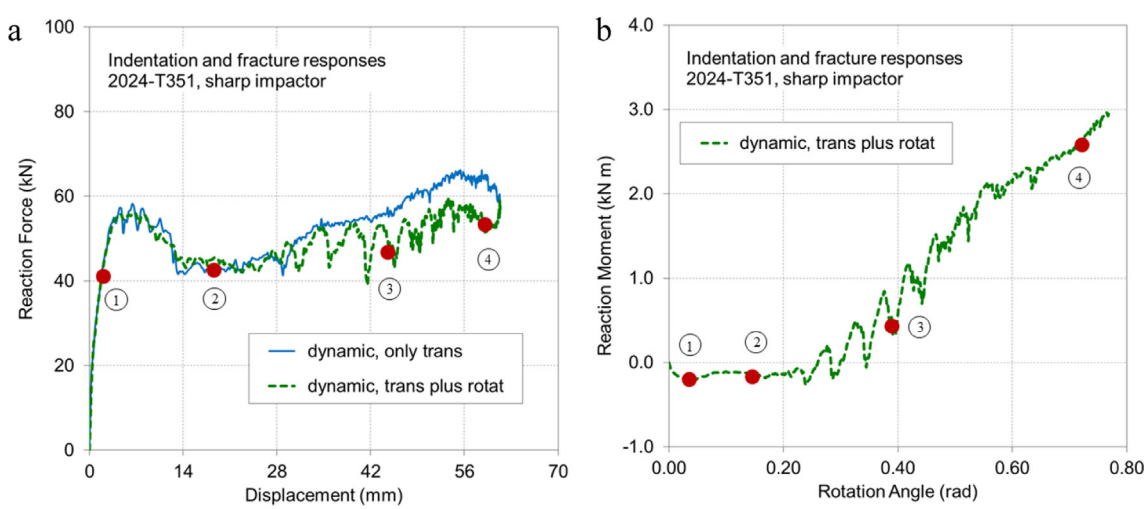

Fig. 30. Global responses of the indentation without and with rotation: (a) vertical resistance force-displacement curves of Case 6-1 and Case 6-3, and (b) resistance moment-rotation angle curve of Case 6-3.

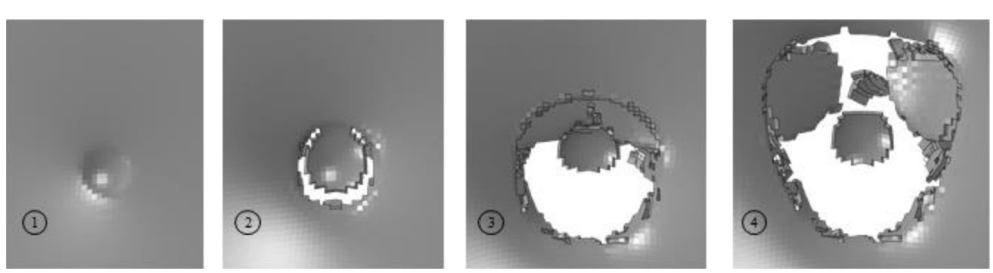

Fig. 31. Armor plate perforation in Case 6-3.

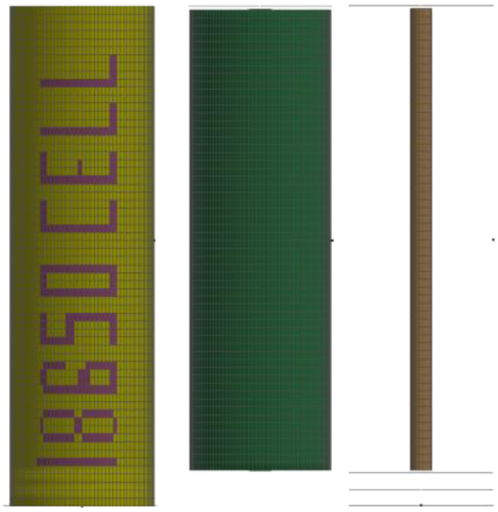

Fig. 32. Components of the finite element model of an 18650 cell, from left to right, the shell casing, jellyroll, and core/end-cap components.

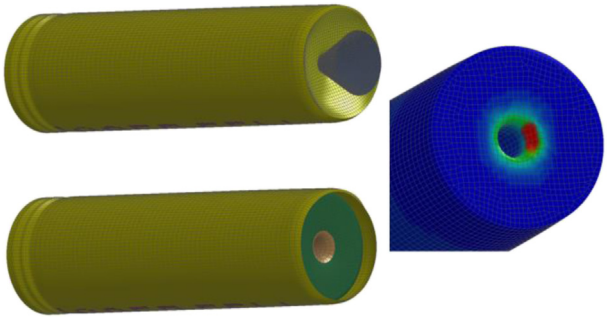

Fig. 33. Cone intrusion in center of the end-cap at a right angle.

other words, to push the punch tip upwards in a same distance, a larger amount of external work (or energy input) is needed to synchronously drive the adjacent area including the nearby battery cells.

As described in Section 2, typical ground impact scenarios often experience rotation of the impacting object rather than purely vertical indentation. To get an initial picture of the rotation effect on the global and local responses of the ground impact, we ran another dynamic simulation (Case 6-3) where the vertical translation of the punch tip (the blue line (in the web version) in Fig. 3a) and the rotation around the punch tip (the blue line (in the web version) in Fig. 3b) are coupled together. Fig. 29 shows the indentation sequence of the battery pack integration in Case 6-3. It is observed that the battery cell above the punch tip presents more prominent oblique posture than that in the purely vertical indentation cases, which is induced by the asymmetric loading due to rotation of the punch tip along with its indentation. In Fig. 30a, the curve of resistance force vs. indentation displacement along the vertical direction in Case 6-3 is compared with that in Case 6-1. The two global response profiles are quite close to each other within the first half stage of the total indentation, while a slight deviation occurs when the indentation becomes larger than 28 mm, implying that the punch tip rotation has a weak effect on the vertical indentation response. It can also be observed from Fig. 30b that the resistance moment imposed on the punch tip in Case 6-3 becomes remarkable when the rotation angle exceeds 15° (0.25 rad), exactly corresponding to the slight deviation stage of the vertical indentation response in Fig. 30a. In the meantime, the perforation of the armor plate in Case 6-3, as shown in Fig. 31, is different from those purely vertical indentation cases in terms of the crack propagation and the final shape and size of the punctured hole.

8. Detailed models and simulation of a single cell

A more refined model of the battery cell was developed using LS-DYNA Software to study the cell deformation and possible failure modes of the battery jellyroll in axial loadings observed in ground impact of vehicles. The model includes separate parts for shell casing, end caps, jellyroll, and the central core of the cell. A frictionless contact is defined on the interface of jellyroll with shell casing and core. The casing is modeled using quadratic shell elements of 0.5 × 1 mm, with a piecewise linear plasticity material model. The jellyroll is modeled using LS-DYNA crushable foam material model with 8 node elements of 0.5 × 0.5 × 1 mm, as explained in Refs. [2–5]. Element erosion with a maximum principal tensile strength criterion is used to predict failure in the jellyroll. Fig. 32 shows the three major components of the cell model, shell casing, jellyroll, central core and end-cap.

Axial loading of cells with three types of indenters were simulated using LS-DYNA. Deformation by a conical punch with a 45°

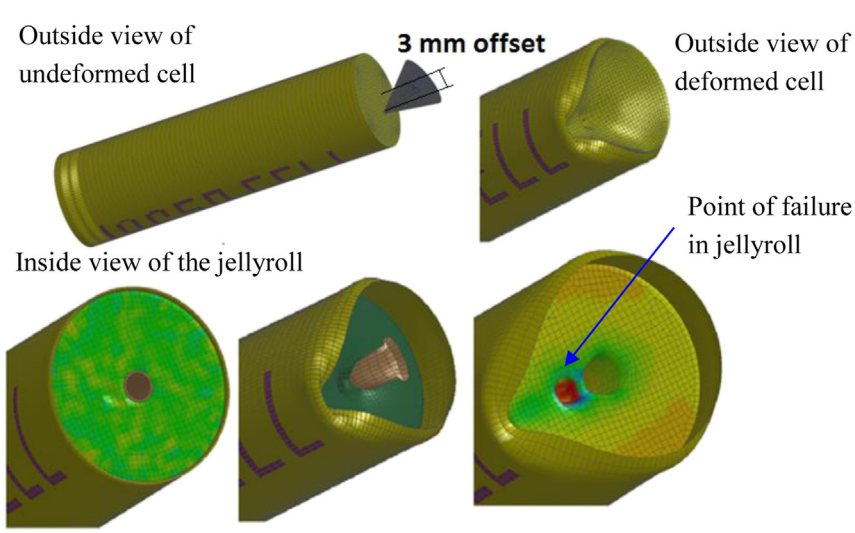

Fig. 34. Conical punch with offset distance and offset angle from axis of the cell.

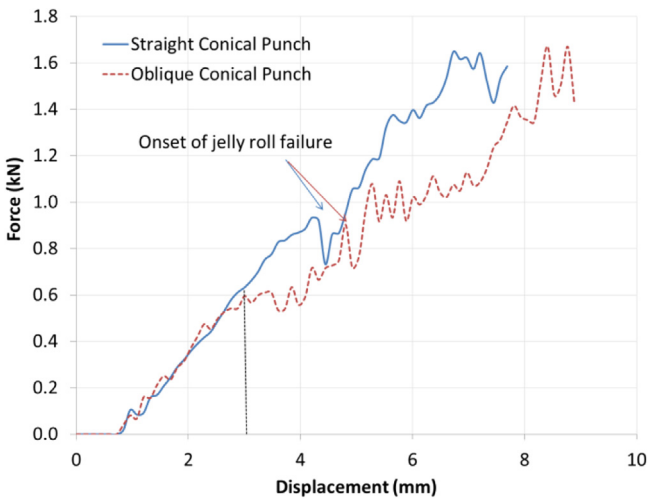

Fig. 35. Force-Displacement due to conical punch intrusion straight at the center (solid line), or oblique with an offset (dash-line).

apex angle was considered first. The cone is modeled in two different configurations, (i) where cone intrusion is at the center of the end cap/core, and cone axis is vertical relative to the end-cap, see Fig. 33; (ii) where the cone tip has a 3 mm offset from central axis of the battery cell, and cone axis has a 20° angle with axis of the cell, see Fig. 34.

The jellyroll failure in these two simulations starts at about 4–5 mm of displacement, the failure areas are shown in red (in the web version) in Figs. 33 and 34. In case of the central loading, with the intrusion of the punch the core starts to deform and opens up pushing sideways to jellyroll and the edge of the central core creates failure in the jellyroll, while in the case of oblique intrusion at an offset, it is the pointed deformation of end-cap that creates large strains and damages the jellyroll.

The force displacements in both cases of conical loading are shown in Fig. 35. The load-displacements for the two loading configurations are the same up to a punch intrusion of approximately 3 mm. After that, the two curves start to diverge. However, the failure of the jellyroll in both cases is the same and starts at about 5 mm of intrusion.

In the third simulation, the cell is compressed between two flat surfaces, see Fig. 36. Such a loading occurs for the cells which are away from the point of local loading, as show in Fig. 17. Nothing significant happens in the simulation, except that the outer shell develops nice axisymmetric folds. Uniform compression of the cell between the two surfaces does not cause any internal failure point in the jellyroll within the present homogenous and isotropic model of the jellyroll. However, the large deformation (bulging) of the core at the end-cap area may result in cell failure at that location.

The corresponding load-displacement, shown in Fig. 37 is similar to the one for crushing of empty thin cylinders, but shows also some differences in the form of prolonged plateau after the first fold.

A much more interesting loading case is shown in Fig. 38 where the cell is subjected to a hemispherical punch loading. Even though the loading is axisymmetric, the response is not. The asymmetry is caused by local buckling of the outer shell at the top. This process is known to be very sensitive to imperfections. The cell starts to shift toward left and the loading becomes unsymmetrical. After that, an axisymmetric fold is formed at the bottom of the cell, and the cell starts to tilt to the right, increasing the amount of asymmetry. This shift in loading causes sidewise deformation of the center core. After 14 mm of deformation, jellyroll elements start to fail, ultimately forming two longitudinal cracks at 15 mm punch intrusion, as shown in Fig. 39. Jellyroll failure may indicate the onset of internal short circuit.

The load displacement in this case, has an original linear part of increasing load which indicates the symmetrical resistance of the shell casing. Then a plateau in the force indicates an area where shell casing has lost its strength due to buckling, and only jellyroll is resisting to the force. Extreme loading of the jellyroll causes stiffening of the material and an area of significant increase in force before the final drop, due to massive failure of jellyroll elements.

9. Detailed simulation of fracture in shell casing of a single cell

Previous work of the investigating team has shown that shell casing contributes little to the resistance of a cylindrical cell when loaded laterally near the center [4]. On the other hand the end cups provide considerable crashing strength in the case of edge loading. In the present architecture of the battery pack, the cells are stacked perpendicularly to the floor and subjected to predominantly axial compression. In the laboratory setting, two failure modes were observed under uniform compression. Initially, the so called concertina folding is developed, Fig. 40.

Upon further compression, the empty space inside the cell is gradually reduced and the compressed jellyroll and electrolyte exert internal hydrostatic pressure causing shell casing to rupture, as shown in Fig. 41, where the numerical simulation of the deformation and fracture pattern is also exhibited.

A high degree of correlation between FE simulation and test was obtained in the course of a very comprehensive experimental and calibration effort of the shell casing material. Interested reader is referred to [13] for detail. The plasticity model is described by

Fig. 36. Deformation of cell axially, between two flat surfaces.

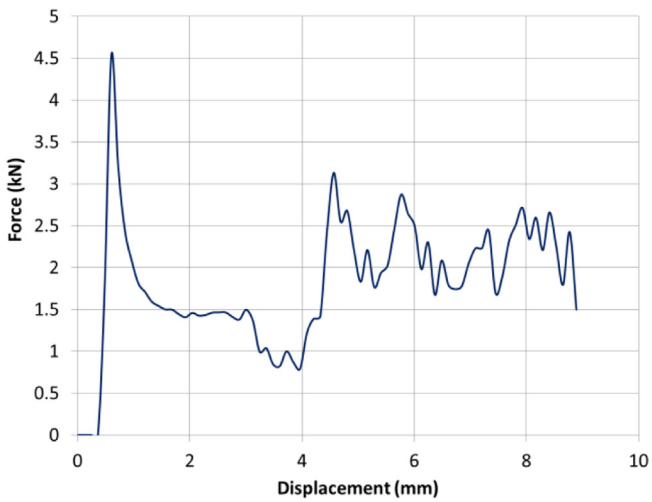

Fig. 37. Force-displacement under axial loading of cell.

- Hill'48 anisotropic yield condition
- Associated flow rule
- Combined Swift and Voce hardening rule to represent the stress–strain curve for large strains beyond necking.

Fracture is defined by the damage evolution rule

$$dD = \frac{d\bar{\varepsilon}}{f(\eta, \theta)} \tag{15}$$

where $d\bar{\varepsilon}$ is the increment of the equivalent plastic strain, and $f(\eta,\theta)$ represents the fracture envelop for proportional loading, according to the triaxiality η and Lode angle θ dependent MMC fracture criterion. The material element is said to fracture when the damage function reaches unity. The crack path is visualized by the process of element deletion. The MMC fracture model was first proposed by Ref. [8] and since then was subjected to numerous validation studies [23,24].

Shell casing is relatively thin with the radius to thickness ratio around 40. Therefore, both solid and shell FE model are adequate for plasticity simulation in the global modeling of the ground impact, while in order to predict the initialization and propagation of the cracks, solid element modeling was used throughout Section 9.

In actual accidents the cells are loaded with some amount of eccentricity or an inclined punch trajectory. The punch tip radius is another parameter for a parametric study. Two load cases were considered in the present study, symmetric local loading and eccentric loading with the same punch tip radius of 10 mm, as shown in Fig. 42.

The amount of eccentricity e is a model parameter which can vary from zero to the outer radius of 18650 cell. Simulations were run for two limiting cases, $e = 0$ and $e = 9$ mm. The welded end caps have quite complicated structure and it was not modeled here. Instead, punch loading was applied from the deep drawn bottom of the can.

Very detailed finite element model was developed with six layers of solid elements through the thickness. The C3D8R solid elements from the ABAQUS library were used with edge dimension of $0.04\times0.08\times0.08$ mm. Totally, there were about 200,000 elements in the model and each run took about 6 h with 6 CPUs. The punch head was modeled as a rigid body and the general contact method was used. Calculation was run until first fracture, which occurred always near the edge of the bottom end cap. The undeformed and deformed geometries of the can in the two cases are respectively shown in Figs. 43 and 44.

The simulation shows that the punch displacement to fracture depends on the amount of eccentricity. The symmetrically loaded can fractures under $\delta_f = 6$ mm indentation while the off-center loaded cell develops fracture at a much smaller penetration of $\delta_f = 1.2$ mm. The above two limiting loading cases cover the entire range of eccentricities. The exact location of the tip of the punch with respect to the cell is a random parameter. The present simulation using an empty shell casing demonstrates the general procedure and it is not aimed at referring to any specific loading cases. However, the general conclusion is very clear: shell casing can fracture under a very small vertical penetration of the punch. More information about the crack propagation could be seen from Fig. 45, showing progressive propagation of the circumferential crack in two above loading cases.

10. Discussion

The paper presented a top-down approach to the analysis of the damage to an integrated battery pack into the vehicle body structure. To narrow down the scope of the paper, a "Floor" architecture of the battery pack composed on 18650 cylindrical cells was assumed. Other design concepts could also be treated using similar methods. The objective of the paper was to develop a general methodology rather than to present a solution to one specific impact situation. Several interesting aspects of the analysis were identified in the body of the paper and the most important one deserves an additional discussion.

The most important issue is the definition of a ground impact. Traditionally a bottom of any car is protected by a sheet of an order

Fig. 38. Axial compression of cell with a hemispherical object.

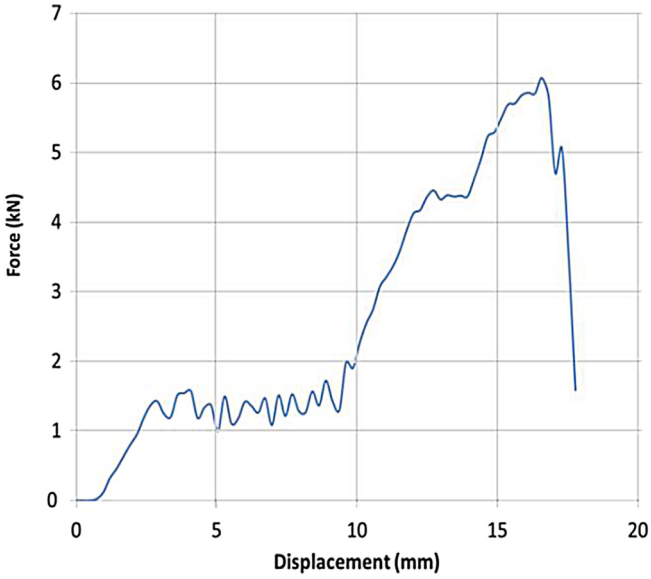

Fig. 39. Force-displacement, due to spherical axial indentation.

of 1 mm thick, coated by polymeric material for rust protection and noise insulation. The floor panel gives an adequate protection against impact of small stone on a gravel road. It is not difficult to put some numbers on the amount of dent assuming a spherical impactor of radius R_b and perfectly plastic material idealization with the flow stress σ_0. The impacting mass is $M = 4/3\pi R_b^3\rho$, where ρ is mass density of the impacting object.

Equating the total kinetic energy of the impacting sphere to the internal plastic work of the plastic membrane, one can derive an approximate solution for the penetration depth

$$\frac{\delta_f}{h_0} = \sqrt{2/3}\ \frac{V}{c}\left(\frac{R_b}{h_0}\right)^{3/2} \tag{16}$$

where $c = \sqrt{\sigma_0/\rho}$ is the reference velocity. Taking for example the mass density of a rock $\rho = 2.5$ g cm^{-3} and $\sigma_0 = 500$ MPa, the reference velocity c is of an order of 500 m s^{-1}. It transpires from Eq. (16) that, unless the stone is very large, the resulting deflection of the floor plate is indeed small. Also, the deflection becomes smaller with increasing plate thickness. The above analysis eliminates the possibility of cell damage due to the impact of flying stones. This leaves the other scenario of kinematically induced indentation, shown schematically in Fig. 2.

From the closed-form solution, Eq. (5), confirmed by the numerical simulation, a critical indentation depth causing fracture of the protective plate was shown to be independent of the plate thickness. It will be approximately the same for 1 mm and 6 mm thickness of the "armor" plate. If the plate thickness is still increased, the car might be lifted without fracture, but this would occur only for a military armor vehicle. Alternatively, a piece of road debris might collapse and crush without inflicting mortal damage to the battery pack. Because of so many possible geometrical characteristics of the road obstacles, it is next to impossible to provide an absolutely impenetrable ground impact protective barrier.

If the bottom protective plate cannot guarantee 100% safety, attention should then be shifted to the design of a floor plate separating modules and cells from the passenger cabin. In the absence of such a plate, the cylindrical (or other types) cells will be just pushed upwards as almost non-deformable rigid bodies. The strength of the floor panel exerts a compressive force on cells causing their shortening and possible thermal runaway. The question that should be posed is to find an optimum design between these two extreme cases. In practice, there must be a floor panel separating lithium-ion cells from the feet of occupants. Therefore, shortening of cells is inevitable. The next question is how much axial compression the cell could withstand before inducing an electric short circuit.

Even though individual cells are the last level of defense against the external loads/indentation, development of simulation tools for designing more impact tolerant cells is not in the mainstream of funded research in the open literature. Limits on the indentation of individual cylindrical and pouch cells under lateral indentation were addressed in a number of publications of the investigating team [2–5]. Those tools and calibrated material constants were tentatively used in the present paper to predict the onset of the electric short circuit under predominantly axial loading. The computational models were derived for a homogeneous and isotropic model of a jellyroll without consideration of the layered structure of the cell interior. An earlier pilot study [5] demonstrated that a system of local wrinkles is developed under in-plane compression, which in addition to membrane stresses induces severe local bending of the electrode/separator assembly. This phenomenon can accelerate the tensile failure of the brittle electrode

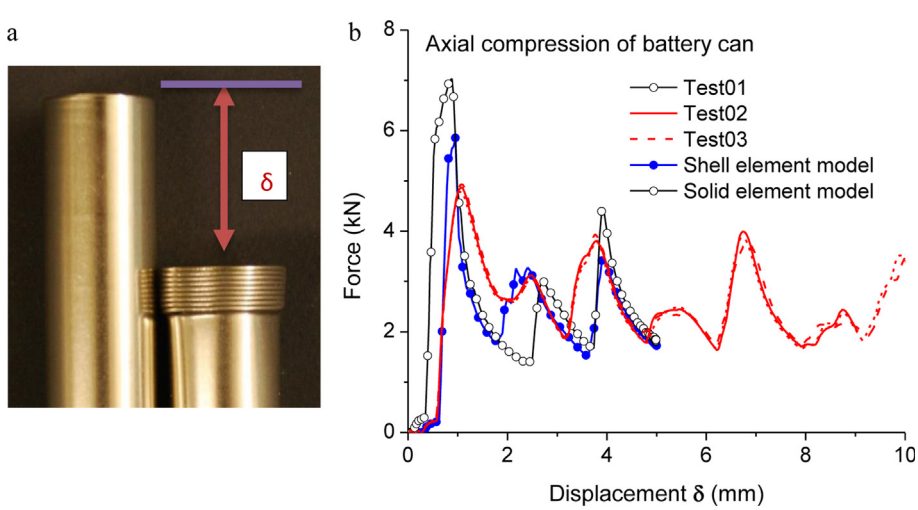

Fig. 40. Concertina folding of an empty can and comparison of test and numerical simulation.

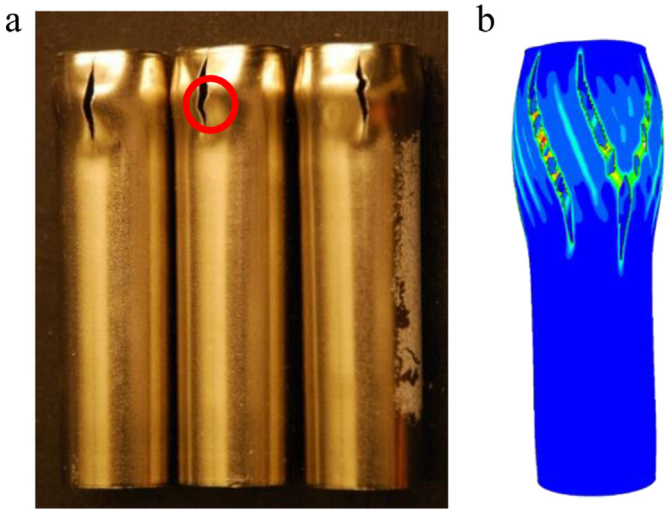

Fig. 41. The shell casing cans burst with building up of internal pressure (left); numerical simulation predicts slightly inclined cracks (right), also shown on the photo.

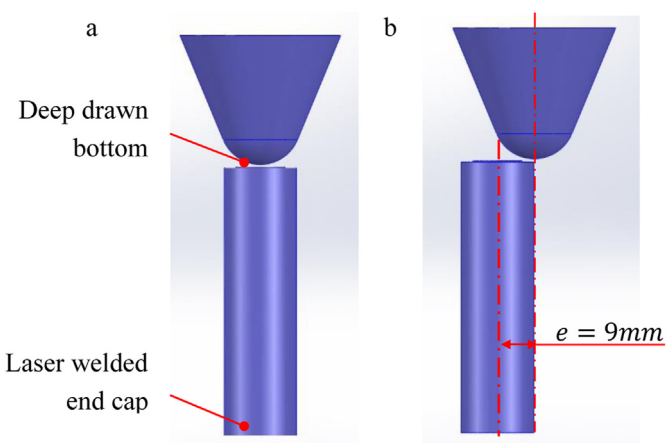

Fig. 42. Symmetric and eccentric loading of deep drawn bottom of empty can.

coating, leading to a premature failure of a separator. A project is underway at MIT on the development of an improved computational model and a calibration procedure for an anisotropic layered structure of the jellyroll.

Another important effect not yet considered is a detailed modeling of end cups, which could be a source of an electric short circuit under certain types of loading directions. Those important topics are actually included in the work plan for the MIT Battery Consortium [25].

11. Conclusions

The present paper presents a multi-scale and multi-material analysis of a very practical and real problem dealing with safety of lithium-ion batteries. Several general conclusions can be drawn from the obtained results.

The present solution has clearly shown that the right design concept of the vehicle integration of the battery pack is a key factor controlling the damage severity of an electric car subjected to a ground impact. The car structural elements such as bottom protective plate, floor panel, transverse cross members, side rails and so on provide various level of protection. They can also endanger the safety level of the battery pack. A compromise must be found between the main role of these members in providing an adequate level of stiffness and strength of a vehicle and an additional role of safe integration with the battery pack. The ultimate solution would require also a careful consideration of different collision scenarios other than ground impact, namely side impact, frontal offset collision etc.

The second general conclusion is that understanding and predicting fracture phenomenon is an indispensable factor of a safe design of an electric car. The most dangerous for inducing an electric short circuit is failure of the separator which, in turn is perpetuated by the fracturing coating of electrodes. These phenomena are happening at the level of 10–100 microns. At the level of a homogenized cell model, fracture of the jellyroll occurs at the scale of a solid element, typically of 1–5 mm. The jellyroll is protected by the shell casing which can either be severely dented or punctured, leading to an immediate short circuit. The next level of protection is offered by the enclosure of modules and pack, which can be either sheet metal of molded plastic. The present analysis proved how easy it is to cut through these members. Finally, ductile fracture of the bottom "armor" plate accelerates the rate of penetration leading to ultimate failure. On the other hand, the fracture strength of the floor panel was shown to act in an opposite direction by relieving pressure on individual cells. No simulation model that does not seriously take fracture phenomenon into account can contribute anything to safe design of a battery pack.

The third general conclusion is that it is not possible with the speed of the present desk computers to develop a single FE model of the integrated battery pack. In the present paper three different models were constructed with decreasing mesh size, the global model with medium size of solid elements and two models of the jellyroll and shell casing with a much smaller element size. The failure of a jellyroll should be determined by computational homogenization of individual layers with element size if one or two

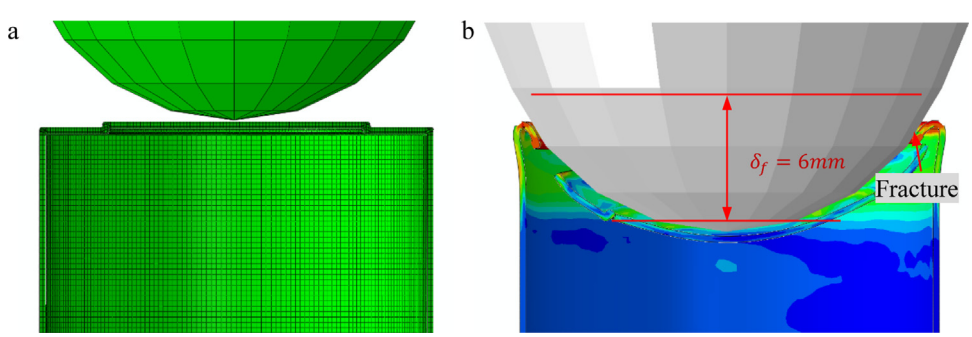

Fig. 43. The undeformed and deformed geometry corresponding to onset of circumferential crack.

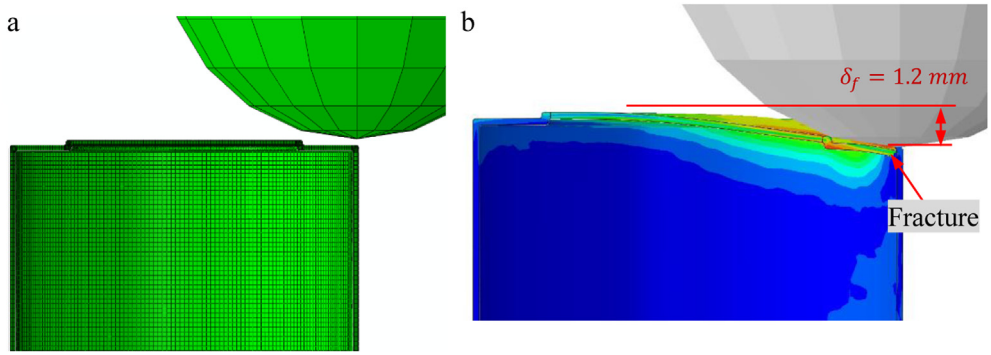

Fig. 44. The undeformed and deformed geometry corresponding to the initialization of edge crack.

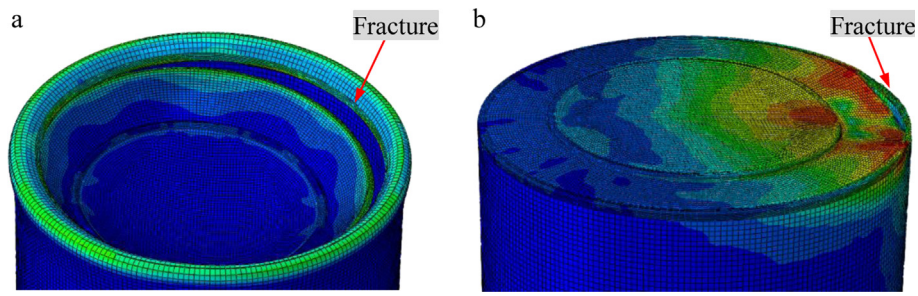

Fig. 45. The 3D view of the fractured can showing the extent of circumferential cracks: (a) symmetric loading case, and (b) eccentric loading case.

orders of magnitude smaller. These observations clearly pose a challenge for the modeling effort, but could be solved and will be addresses in the course of continuing research of the investigating team.

Several more specific lessons were learnt from the presented results. One was a proper balance between strength and ductility. The use of high strength aluminum alloys or steels increases the resisting force but produces dangerously sharp edges of cracks that could puncture cells more easily than the blunt edges of road debris. Also it was shown by the analytical solutions as well as FE simulation that the onset of fracture of the armor plate is independent of the plate thickness. This observation brings a very important question of optimum design of protective structure. From the list of candidates are monolithic plates, plates on polymeric or foam foundations, sandwich plates and their combination. These issues will be resolved in future publication of the investigating team.

References

[1] B. Smith, Chevy Volt Battery Incident Summary Report, Report Number: DOT HS 811573, 2012.
[2] E. Sahraei, J. Meier, T. Wierzbicki, J. Power Sources 247 (2014) 503–516.
[3] T. Wierzbicki, E. Sahraei, J. Power Sources 241 (2013) 467–476.
[4] E. Sahraei, J. Campbell, T. Wierzbicki, J. Power Sources 220 (2012a) 360–372.
[5] E. Sahraei, R. Hill, T. Wierzbicki, J. Power Sources 201 (2012b) 307–321.
[6] X. Teng, T. Wierzbicki, Comput. Struct. 83 (2005a) 989–1004.
[7] X. Teng, T. Wierzbicki, Int. J. Impact Eng. 31 (2005b) 667–698.
[8] Y. Bai, T. Wierzbicki, Int. J. Fract. 161 (2010) 1–20.
[9] X. Teng, S. Dey, T. Borvik, T. Wierzbicki, J. Mech. Mater. Struct. 2 (2007) 1307–1328.
[10] Y.W. Lee, J.C. Woertz, T. Wierzbicki, Int. J. Mech. Sci. 46 (2004) 751–781.
[11] A.M. Beese, D. Mohr, Exp. Mech. 51 (2011) 667–676.
[12] M. Dunand, D. Mohr, Int. J. Solids Struct. 47 (2010) 1130–1143.
[13] X. Zhang, T. Wierzbicki, J. Power Sources (2014) submitted for publication.
[14] Aerospace Specification Metals, Inc, http://www.aerospacemetals.com/index.html.
[15] G. Gu, Y. Xia, C.H. Lin, S. Lin, Y. Meng, Q. Zhou, Mater. Des. 44 (2013) 199–207.
[16] S. Lin, Y. Xia, C.H. Lin, J. Wang, G. Gu, Stress state dependent failure loci of a talc-filled polypropylene material under static loading and dynamic loading, in: 13th International Conference on Fracture, June, 2013, Beijing, China, 2013.
[17] Dassault Systèmes Simulia Corp., 20.3.5 Crushable foam plasticity models, in: ABAQUS 6.10 Analysis User's Manual, Providence, RI, USA, 2010.
[18] V.S. Deshpande, N.A. Fleck, J. Mech. Phys. Solids 48 (2000) 1253–1283.
[19] Dassault Systèmes Simulia Corp., 3.2.7 Simple tests on a crushable foam specimen, in: ABAQUS 6.10 Benchmarks Manual, Providence, RI, USA, 2010.
[20] B.C. Simonsen, L.P. Lauridsen, Int. J. Impact Eng. 24 (2000) 1017–1039.
[21] T. Wierzbicki, Petalling of plates under explosive and impact loading, Int. J. Impact Eng. 22 (1999) 935–954.
[22] Y.W. Lee, T. Wierzbicki, Int. J. Impact Eng. 31 (2005) 1277–1308.
[23] Y. Li, T. Wierzbicki, M. Sutton, J. Yan, X. Deng, Int. J. Fract. 168 (2010) 53–71.
[24] K. Pack, M. Luo, T. Wierzbicki, Sandia fracture challenge: blind prediction and full calibration to enhance fracture predictability, Int. J. Fract. (2014), http://dx.doi.org/10.1007/s10704-013-9923-3.
[25] T. Wierzbicki, E. Sahraei, 4th MIT Workshop on Computational Modeling of Lithium-ion Batteries, MIT, 2013.